FORMATION OF PHYSICAL SEDIMENTARY STRUCTURE IN THE PRESENCE OF MICROBIAL COMMUNITIES

A Dissertation

by

JIAN GONG

Submitted to the Office of Graduate and Professional Studies of
Texas A&M University
in partial fulfillment of the requirements for the degree of

DOCTOR OF PHILOSOPHY

Chair of Committee,	Michael M. Tice
Committee Members,	Thomas D. Olszewski
	Michael Pope
	Scott A. Socolofsky
	Daniel Conrad O. Thornton
Head of Department,	Michael Pope

December 2015

Major Subject: Geology

ABSTRACT

Microbial life has been fundamental in the evolution of the Earth throughout geologic time. Although insignificant as individuals, collectively as communities microorganisms impact sedimentary environments by producing physically resilient structures. Many of these sedimentary structures, when understood in specific contexts, may serve as unique records for ancient life.

Conical mats are some of the most distinctive fossil microbial communities in the geologic record. However, much is debated about how they form. We here show with experimental evidence that cones constructed by *Leptolyngbya* sp. occurs by repeated aggregation of mobile filaments likely coordinated by physical contact. Cone-forming cultures also rolled underlying sand grains into small piles beneath each biological cone. Repeated rolling over multiple day/night cycles gradually sorted sand into regularly spaced coarse piles with finer-grained lags in between. Significantly, statistically identical sorting patterns were discovered in 3.22-billion-year-old fossil conical mats that grew in sandy tidal environments of the Moodies Group, South Africa. These results demonstrate that group movement coordinated by touch-sensing systems could have structured populations of filamentous, photosynthetic microorganisms since at least the Paleoarchean.

Microbial streamers are surface-attached microbial communities that paradoxically seem to roughen mats under rapid, high shear flows, potentially exposing the community to greater risk of erosion. They are common structures found in fast flow

environments yet the mechanism of their formation and effects on mat erosion are poorly understood. We here show evidence that streamers are initiated by shear-induced viscoplastic deformation, and they locally re-attach boundary layers and therefore smooth rough bedding surfaces hydraulically, reducing shear experienced by near-surface mat communities. These results suggest a novel set of feedbacks that could reduce net mat erosion in energetic flows, and could help guide the evaluation of biosignatures in sedimentary rocks deposited in the presence of microbial mats.

The presence of microbial communities have long been suggested to cause the increase of sediment cohesive strength, which is responsible for forming a wide range of microbial-sedimentary structures. Step-wise increase of mat strength towards the end of Archean has been documented, but it is uncertain what caused this change. We here suggest that the mechanical strength of mats increased as a direct product of the metabolic switch from an anoxygenic to oxygenic benthic microbial ecosystem. Support for this hypothesis is provided by examining the strength of experimental mats with productivity limited by various nutrients. In addition, we also expand the record of estimated mat strength beyond the Archean eon. These results add to a growing body of evidence how one single metabolic innovation – oxygenic photosynthesis forever altered the face of our planet.

DEDICATION

To Earth, which harbors and defines life.

To us born explorers, who shall never rest still.

ACKNOWLEDGEMENTS

I thank my committee chair, Dr. Tice, for guiding me through uncharted territories in intellects and in life, for his patience and support so I grew to become a better thinker. My gratitude also goes equally to the committee members, Dr. Thornton, Dr. Pope, Dr. Olszewski, and Dr. Socolofsky, for their teaching, expert knowledge and support throughout the course of my research.

Thanks also go to my big family at the Department of Geology and Geophysics, Texas A&M University, who made my research life a great experience. I also want to extend my gratitude to the Berg-Hughes Center for funding my graduate research.

Finally, thanks to my mother and father for their love and encouragement, to my wife Ama for her patience and unyielding love, and to my 1-year-old son, Teo, for his inspiration before he even fully understands it.

NOMENCLATURE

GOE	Great Oxygenation Event
EPS	Extracellular Polymeric Substances
XRF	X-Ray Fluorescence
PIV	Particle Image Velocimetry
PTV	Particle Tracking Velocimetry
TES	2-{[tris(Hydroxymethyl)methyl]amino}ethanesulfonic Acid
VWR	VWR International, LLC.
SATP	Standard Ambient Temperature and Pressure (25 °C and 1 bar)
FPS	Frames per second

TABLE OF CONTENTS

LIST OF FIGURES

LIST OF VIDEOS

CHAPTER I

INTRODUCTION

Microbially induced or influenced sedimentary structures are long-standing puzzles in physical sedimentology, because the formation of these features is either hard to explain or could be explained by many alternative theories. Although biology is not expected to defy physics, every now and then, it manages to do a little magic by producing peculiar shapes in sediments. These curious shapes, including cones, domes, columns, irregular laminations, puzzling grain sortings and more, accumulate as potential evidence of life in the geologic record. The questions such as “what specific biological or environmental significance do these shapes represent” and “how and why do they form” are the central themes that motivate this research.

Traditional physical sedimentology focuses on the first order principles by which sediment get eroded, transported and deposited, within which biological processes are largely ignored. There are several notable reasons why this is the case. First is that biological processes are generally complex and highly coupled to other chemical or physical processes, so factors that constrain these processes are difficult to define. Secondly, growth, motility and metabolism are activities commonly maintained by individual organisms. However, when microorganisms share resources and live together as communities, many of these rules change and differentiate spatially and temporally in response to external environments. Therefore, without a good grasp on the emergent properties of a complex system and a unified scheme to generalize, physical problems

become overly-simplified.

However, this ignorance of biological processes does not mean that they are irrelevant. On the contrary, just about everywhere we look, from the top of glaciers to deep within the continental crust, we find the presence and influence of life (Skidmore et al. 2000; Lin et al. 2006). As a result, life has become a geologic force that affects every major modern surface process on Earth (Westbroek 1983). As far back as we can examine in the geologic record, microorganisms already took hold and built elaborate structures, influencing sediment deposition and transport (Allwood et al. 2006; Heubeck 2009). Throughout the history of our planet, life has coevolved with larger environments, affecting its path of evolution every step of the way (Dietrich et al. 2006).

For the majority of recorded history of our planet, life on Earth was dominated by microorganisms (Knoll et al. 2012). These tiny but abundant organisms, in the interest of their own survival, collectively altered the chemical redox state of the planet surface through geologic time, eventually leading to the recent evolution and radiation of diverse morphological traits such as higher plants and animals. However, details about the history of microorganisms are difficult to interpret due to lack of fossilized organisms, partially due to degradation and diagenesis in sedimentary rocks. As a result, besides extracting interesting chemicals and measuring isotopic signals, information such as larger scale morphological characters of microbial sediments are often the only material we have to work with.

Recent investigations on the morphology of microbial sediments hint that fluid interaction with surface microbial communities could be the key to understanding how

microbial sediments evolve shapes (Tice et al. 2011). Central in this model is the idea that structures of any turbulent environmental flow may be subdivided into a diffusive boundary layer right next to the surface and a well-mixed turbulent layer away from the surface. Within the diffusive boundary layer, the flow is laminar and transport is dominated by diffusion. As a relatively slow transport process, diffusion ultimately limits the nutrient or waste transport for microorganisms living on surfaces. This means that communities situating higher on local topography obtain better exchange with the environment, accumulating more biomass to become even higher. Thus, diffusion here provides a mechanism for differential growth necessary to enhance surface topography. However, a closer examination on how cyanobacteria form conical structures in diffusion-dominated environments has resulted in some striking discoveries on the active motility and social organization of these microorganisms in additional to the previously-believed passive growth. This work is detailed in Chapter II.

Following the same model, turbulence away from the boundary layer is well-mixed but erosive, which when acting over certain topography, generally causes enhanced erosion of protruding tops, resulting a general reduction of surface topography. However, this prediction seems to contradict the observation that certain microbial structures called streamers are commonly found in erosive channel flows. A detailed examination on the formation of microbial streamers revealed that upon erosive forcing, in contrast to inorganic sediments, microbial mats may slowly deform like a fluid rather than being removed. This observation, detailed in Chapter III, not only explains how streamers initiate, but also reveals that these structures could act to re-attach separated

boundary layers and hydraulically smooth the flow. As the hydraulic roughness of the mat surface reduces, near surface erosion also lessens because the boundary layer is lifted to on top of the streamers. This is likely a common process by which mats engage with fluid erosion.

Finally, a challenging but core component of the surface evolution model is to evaluate the emergent material properties of sediments when they are inhabited by microbial communities. This is because the cohesion of sediments, although invisible, interacts intimately with external physically forcing, dictating how growth and erosion may proceed, permitting various structures to be sustained and preserved. More importantly, because these physical material properties are quantifiable, we may estimate the record of mat cohesion from ancient rocks. In Chapter IV, the mat strength record is expanded beyond the Archean eon, and modern culture experiments are applied to better understand how the step-wise increase of mat strength towards the end of Neoarchean could be linked to the expansion of oxygenic photosynthesis.

CHAPTER II

FORMATION OF CONICAL MATS BY SOCIALLY MOTILE FILAMENTOUS BACTERIA BY 3.22 BILLION YEARS AGO

II.1 OVERVIEW

Fossil conical microbial mats are ancient and morphologically distinctive structures in the record of early life on Earth (Allwood et al. 2006; Flannery & Walter 2012). Experiments with modern cone-forming communities suggest that cones form in response to growth in stagnant fluids where slow diffusive transport limits the exchange of nutrients and wastes with the environment (Petroff et al. 2010), although it is not clear how microorganisms organize themselves to form these structures. Here we show that cone formation in experimental biofilms constructed by *Leptolyngbya* sp. occurs by repeated sticky random walks of groups of tens to thousands of individuals coordinating by physical contact. Cone-forming cultures also rolled underlying sand grains into smaller piles beneath each cone. Repeated rolling over multiple day/night cycles sorted sand into regularly spaced coarser piles separated by finer-grained lags. Statistically identical sorting patterns occur in 3.22-billion-year-old fossil conical mats that grew in sandy tidal environments (Moodies Group, South Africa). These results suggest that motile filamentous photosynthetic bacteria capable of touch-based social organization could have been significant components of the benthic microbiota since at least the Paleoarchaean, and demonstrate the antiquity of an important mode of bacterial multicellularity.

II.2 INTRODUCTION

The early record of life on Earth is dominated by structures built by microbial communities (Bosak et al. 2009; Lowe 1980; Hofmann et al. 1999). Conical mats and stromatolites are particularly ancient and morphologically distinctive features among biosedimentary structures (Allwood et al. 2006). Experiments with cone-forming cultures suggest that they may form in response to growth in stagnant fluids where slow diffusive transport limits the exchange of nutrients and wastes with the environment (Petroff et al. 2010) and that specific associations between heterotrophic bacteria and oxygen-producing cyanobacteria may be critical in mediating cone development (Sim et al. 2012). However, the biological and evolutionary significance of these structures remains unclear because the specific mechanisms structuring conical mats are not yet known.

II.3 RESULTS AND DISCUSSION

II.3.1 Modern Conical Microbial Mats

In order to investigate the processes involved in cone formation, we grew culture of a filamentous cyanobacterium originally isolated from tufted cones in Yellowstone National Park, Wyoming, U.S.A. (*Leptolyngbya sp.* Y-WT-2000 Cl 1, Culture Collection of Microorganisms from Extreme Environments culture number 5627) on acid-washed quartz sand surfaces. Although experimental conical mats are not stromatolites because they are neither lithified nor laminated, understanding how microbial communities initially organize into cones has been a critical goal in

constructing models of conical mat and stromatolite formation (Petroff et al. 2010a; Walter et al. 1976). *Leptolyngbya sp.* is likely a primary cone former in Yellowstone hotsprings (Walter et al. 1976; Reyes et al. 2013; Lau et al. 2005; Bosak et al. 2012), although this does not exclude shared or convergent traits that might enable other bacterial communities to form similar structures. Axenic cultures were grown in shallow, stagnant media open to the atmosphere through a loose-fitting cap. Illumination occurred during a 12-hour period on a regular 24-hour-long day/night cycle. BG-11 (Castenholz 1988) buffered by 10 mM TES was used as a medium, and cultures were grown at 42°C. Under these conditions, conical mats consistently formed after 4-6 weeks of incubation (Figure 2.1). Formation of cones in pure cyanobacterial culture suggests that conical stromatolites do not necessarily imply oxygen production in conjunction with localized heterotrophic aerobic respiration (Sim et al. 2012).

Microscopic time-lapse videos showed that culture cones were formed by gradual accumulation of randomly walking bundles of mutually aligned filaments (tufts) during repeated day/night cycles (Gong et al. 2015). During the first ten days of incubation, filaments reproduced and spread on solid surfaces, forming 100 to 200-μm-long tufts that extended perpendicularly from individual sand grains (Figure 2.2A). Tufts were mobile, bridged sand grains, merged to form larger tufts, and shrunk and disaggregated at night (Video 2.1). During the next two to five days of incubation, tufts grew and merged upon contact to form larger cones spanning several sand grains, together with 1-2-mm-long horizontally radiating “star arms” (Figure 2.2B). Cone activity continued to follow a regular day/night cycle (Figure 2.2C-J and Video 2.2).

During the first hour of morning illumination, rounded and bulbous clumps and loose bacterial masses aggregated upon contact into tufts that rapidly merged to form compact cones and star arms. For the middle nine hours of the illumination period, cones moved randomly across the sediment at rates of up to 10 μm s^{-1} until their star arms made contact, at which point they merged along bridging star arms to form larger cones (Figure 2.2E-H). Cones sometimes split when connected to cones on opposite sides (Figure 2.2D-F). During the final hours of illumination, cones slowed and partially disaggregated as bacteria flowed away from them in streams, leaving smaller bulbous masses (Figure 2.2G-J). Little to no motion occurred at night. Individual cones increased in size over several days, and the number of cones in the culture increased over the next two weeks of incubation.

At approximately four weeks of incubation, the solid substrate was covered by a network of regularly spaced 3 to 5-mm-high cones connected by bridging star arms. Cones became almost immobile, did not disaggregate significantly in the evening, and were crowned by waving tufts (Figure 2.1B and Video 2.3). The motion of tufts within these cones continued to follow a day/night cycle. Cones began each day with crowning tufts arranged in loose, low density heads. Within the first 30 minutes of illumination, these heads contracted and tufts began to wave and rotate. Net rotation over the course of the day wound tufts around each other, effectively growing the underlying cones (Figure 2.1C and Video 2.4). The tops of cones loosened and partially unwound overnight into puffy heads by the next morning.

In order to describe the collective motion of bacterial filaments in tufts, we

observed cultures microscopically during the first 10 to 15 days of development. Tufts anchored to sand grains by attaching the terminal ends of many filaments to the sand surface (Figure 2.3A). Tuft shafts thickened slightly away from their bases because they typically contained many more individual filaments than those maintaining attachment. Free ends tapered to points beyond which 1-3 filaments protruded up to 30-40 μm, rotating and whipping about the end of the more slowly waving tuft. When these extending filaments contacted other tufts obliquely or along their shafts or when they touched sand surfaces, basal filaments detached and the entire tuft moved, either merging with the other tuft (Figure 2.3B) or attaching to the mineral surface. Once cones began aggregating, longer horizontal tufts (star arms) formed and anchored to cones with free ends whipping across the sand or agar surface. Contact with the shafts of other star arms caused connecting arms to merge by wrapping around one another (Figure 2.3C-D), at which point individual filaments began gliding toward the other cone, sometimes dragging the anchored cone behind. In comparison to other known bacterial processes, aggregation in our experiments is most similar to other socially motile bacteria such as myxobacteria (Sozinova et al. 2005) and bacilli (Branda et al. 2001) which regulate motion in response to contact with bacteria of the same species. The presence of such systems was also recognized by the occurrence of travelling waves in dense streams formed during dispersion of cones in *Leptolyngbya* cultures growing on smooth agar (Video 2.5 and Video 2.6).

The mechanisms observed to produce cones in our experiments can produce scaling patterns observed by other investigators that were interpreted to result from

diffusion-limited growth, in particular that cone size and spacing are proportional to the square root of illuminated daylight time (Alexander P. Petroff et al. 2010a). A simple model of cone aggregation as a sticky two-dimensional random walk during the day followed by the partial disaggregation of cones at night predicts an average cone radius r_n after n days of

$$r_n = \sqrt{\frac{4DT\left(1-\beta^{2n}\right)}{1-\beta^2}},$$

where β is the average fraction of cells that do not disaggregate at night and D is a constant that depends on the density of cells in and out of the cones and on the rate of cone migration (see derivation of the model in Appendix A3). For $\beta < 0.9$, the average radius approaches the limiting size of $r_\infty = \sqrt{4DT/(1-\beta^2)}$ in less than eight days, and the observed cone size and spacing is proportional to $T^{1/2}$. For $\beta = 0.5$, or the approximate inheritance observed in our experiments, limiting size is approached in two days. This rapid approach to final cone size is observed in our experiments.

This model also correctly predicts the centimeter-scale size and spacing for cones in a wide variety of modern and ancient examples given realistic model parameters. Since limiting size is relatively insensitive to different β except under cases of very large inheritance of cone size from evening to morning not observed during this study, we assume $\beta \approx 0.1\text{-}0.9$. For realistic values of D (Appendix A3) and $T \approx 1\text{-}4\times10^4$ s, limiting average cone size is about 2-30 mm, and the limiting spacing is 4-70 mm for densely packed cones. These size ranges are commonly observed in the geologic record of fossilized tufted conical mats (Petroff et al. 2010b).

When grown on sand, *Leptolyngbya* cultures moved individual sand grains by gradually rolling them between migrating cones (Video 2.7). In particular, when bridging tufts formed between cones, the grain rolled toward the nearest cone while the cone was also dragged toward it. This observation implies that bacteria in the bridges exerted a net contracting force between the two ends, likely as individuals glided toward each other and the connecting arm shortened. Therefore, sand grains were rolled as a byproduct of group movement between cones. The net product of this motion was that the sand beneath cones was arranged into piles up to 3 mm tall (Figure 2.4), whereas sand surfaces beneath mats at the margins of the experimental flask remained flat.

Because grains are moved when bridging tufts contact their tops, we predict that larger grains that protrude above the average sand surface would be more frequently rolled than finer grains, and that cone aggregation would therefore sort sandy surfaces into coarse mounds and fine troughs. Indeed, grains within cones were on average 12% larger than grains in the bulk substrate ($p = 3.5\times10^{-4}$ for a two-tail t test) and grain diameters decreased systematically with increasing distance from cone centers (p = 0.003 for the coefficient of an ordinary least squares regression of log-transformed grain diameter on distance from the nearest cone apex). This degree of sorting represents an increase in mean grain diameter equivalent to half the overall variation in the starting population (0.52σ).

II.3.2 Comparison with Fossil Conical Mats

In order to compare to grain sorting patterns developed within microbial mats growing in sandy environments in the past, we measured grain size distributions and mapped grain compositions in fossil microbial mats of the 3.22 billion-year-old Moodies Group (Heubeck 2009). Mats in this unit were preserved as rare to abundant, laterally continuous, flat, wavy or crinkly kerogenous laminae less than 1 mm thick. They also cover former bedding planes and foresets in medium-to coarse-grained quartz-rich sandstone interbedded with thin pebble to cobble conglomerates. Microbial mats branch and lap onto underlying relief and clearly formed a microrelief that affected sand transport (Heubeck 2009; Gamper et al. 2012). Specific microbial mat morphotypes dominated by flat, wavy and tufted morphologies, respectively, represent specific tidal depositional sub-environments.

Sand-size quartz and feldspar grains within cones of Moodies Group biolaminated sandstone are visibly coarser than grains in flanking flat laminations, and the rate of change in grain size with distance from the cone center is indistinguishable from that observed in experiment (Figure 2.5). In contrast, smaller and denser zircon and rutile grains are commonly enriched on the tops of flat laminations but absent within and on top of neighboring cones (Figure 2.5). 16 studied cones had neighboring flat mats enriched in zircon and rutile grains, and 15 of these cones were themselves depleted in those grains. An additional 13 cones were not associated with heavy-mineral-enriched flat mats (Figure 2.6 and 2.7). Dense minerals are commonly concentrated in the tops of modern microbial mats, possibly because of differential trapping and binding (Gerdes et

al. 2000). The paucity of heavy minerals within most cones is therefore striking and best explained by shadowing of the finer grains by larger quartz and feldspar grains as sand was rolled into cones. Zircon and rutile grains may also have been enriched in flat regions of Moodies Group microbial mats in part by removal of coarser grains during repeated migration of socially organized bacteria. In either case, the observed preferential accumulation of coarse grains in topographic highs and of dense, smaller grains in topographic lows is inconsistent with sorting by currents (Slingerland & Smith 1986; Cheel 1984); it instead implies a preferential construction of conical mounds from the coarsest grains in Moodies Group sands. This pattern of grain sorting by size and density will potentially be observable by instruments in the planned scientific payload for the Mars 2020 mission (Allwood et al. 2012), and could therefore serve as a test of the biogenicity of putative microbial mat features in sandstone beds (Noffke 2015).

Rolling 150 to 500 μm diameter sand grains over 110 μm grains (as in the Moodies Group examples analyzed here) requires a force of approximately 7-100 nN applied across their top surfaces (see calculations in *Supplementary Material*). Modern bacteria can generate up to 0.1 nN during movement on surfaces (Balagam et al. 2014), suggesting that hundreds of bacteria moving in concert were necessary to sort Moodies Group sand. Moreover, significant sorting in experimental cones developed only over multiple cycles of aggregation and disaggregation, and it is unlikely that sorting by this mechanism could be significantly more efficient. Sorting in Moodies deposits thus reflects repeated cycles of reworking by bacteria during times between sand depositions. These lamina likely formed in shallow intertidal to supratidal environment (Heubeck

2009), so sand deposition was likely related to weekly-to-monthly tidal cycles, and bacterial cycles were most likely diurnal. Together with the restriction of Moodies Group fossil mats to photic-zone shallow-water environments (Noffke et al. 2006; Heubeck 2009) and the evidence for autotrophically-fixed organic carbon (Noffke et al. 2006; Gamper et al. 2012), these traces of diurnal group migration constitute compelling evidence for the extensive colonization of a 3.22 Ga sandy tidal environment by photosynthetic bacteria. It also implies the evolution of socially-coordinated motility in bacteria by the end of the Paleoarchean.

II.3.3 Figures

Figure 2.1. Experimental cones formed from axenic culture. (A) Regularly-spaced eight-week-old cones. (B) Four-week-old stable cone crowned with waving tufts in the middle of the day. (C) Eight-week-old mature cones covering sand surface. All scale bars = 3 mm.

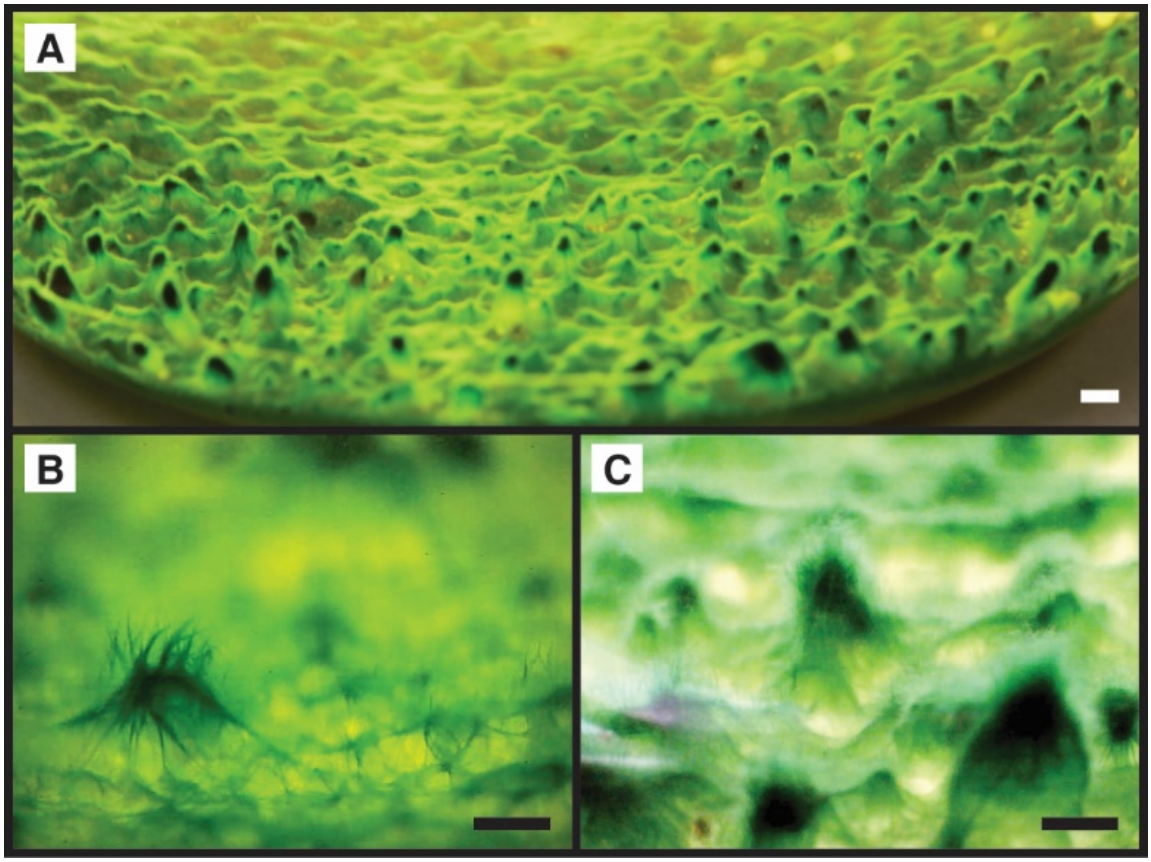
A
B
C

Figure 2.2. Formation of cones on sand surfaces. (A) Bundles of filaments (tufts) standing up from individual sand grains during early incubation. Scale bar = 500 µm. (B) Tufts merged to form small cones. Scale bar = 500 µm. (C-J) Top-down-view time series of cones on sand surfaces over one day. Arrows indicate cones involved in mergers [red] and splits [yellow]. Cones aggregate in early mornings and partially disaggregate in early evenings [blue]. For the corresponding video see Video 2.2. Scale bars = 5 mm. Clock indicates time progression through illuminated time period.

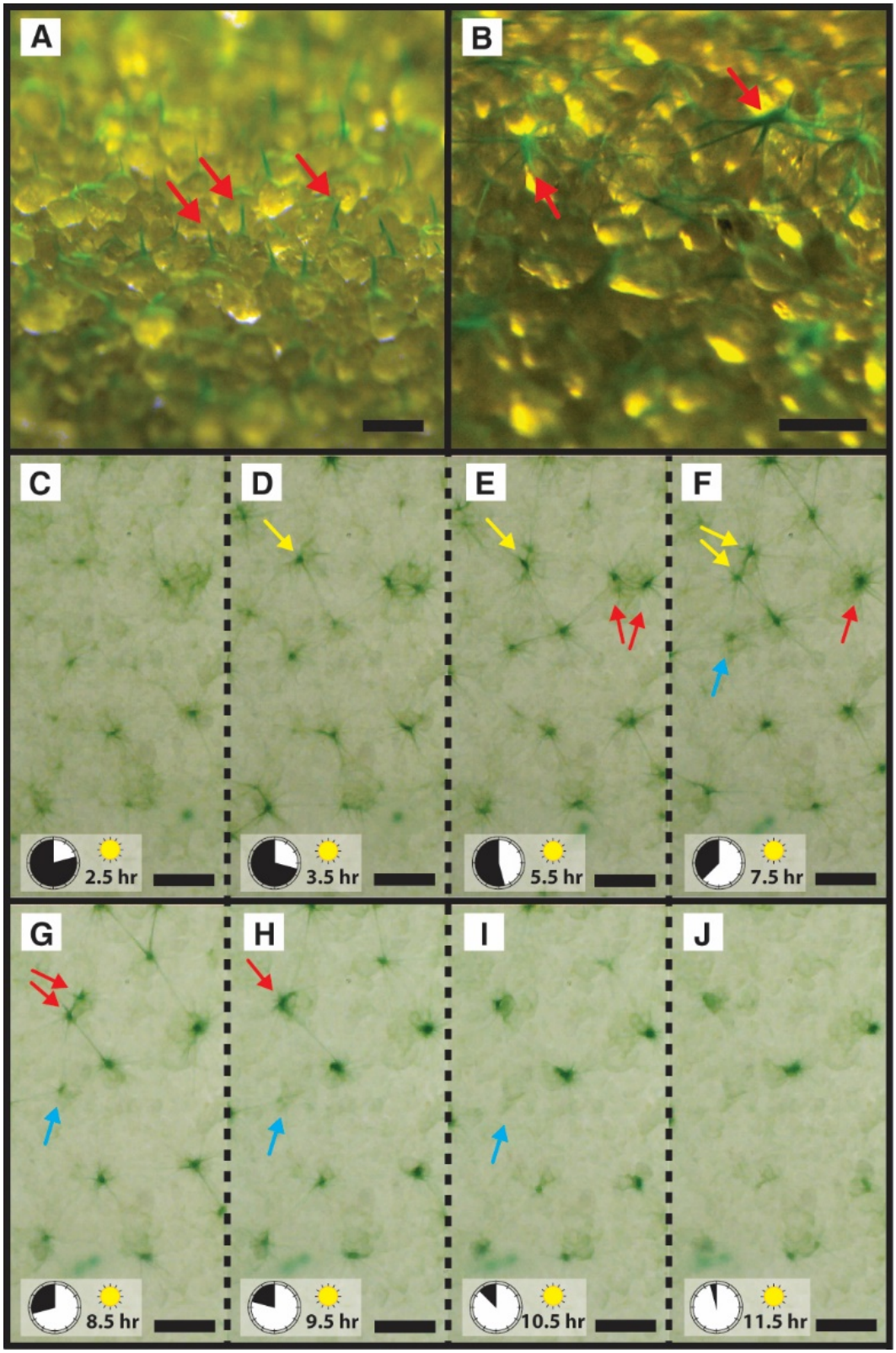
A
B
C
D
E
F
2.5 hr
3.5 hr
5.5 hr
7.5 hr
G
H
I
J
8.5 hr
9.5 hr
10.5 hr
11.5 hr

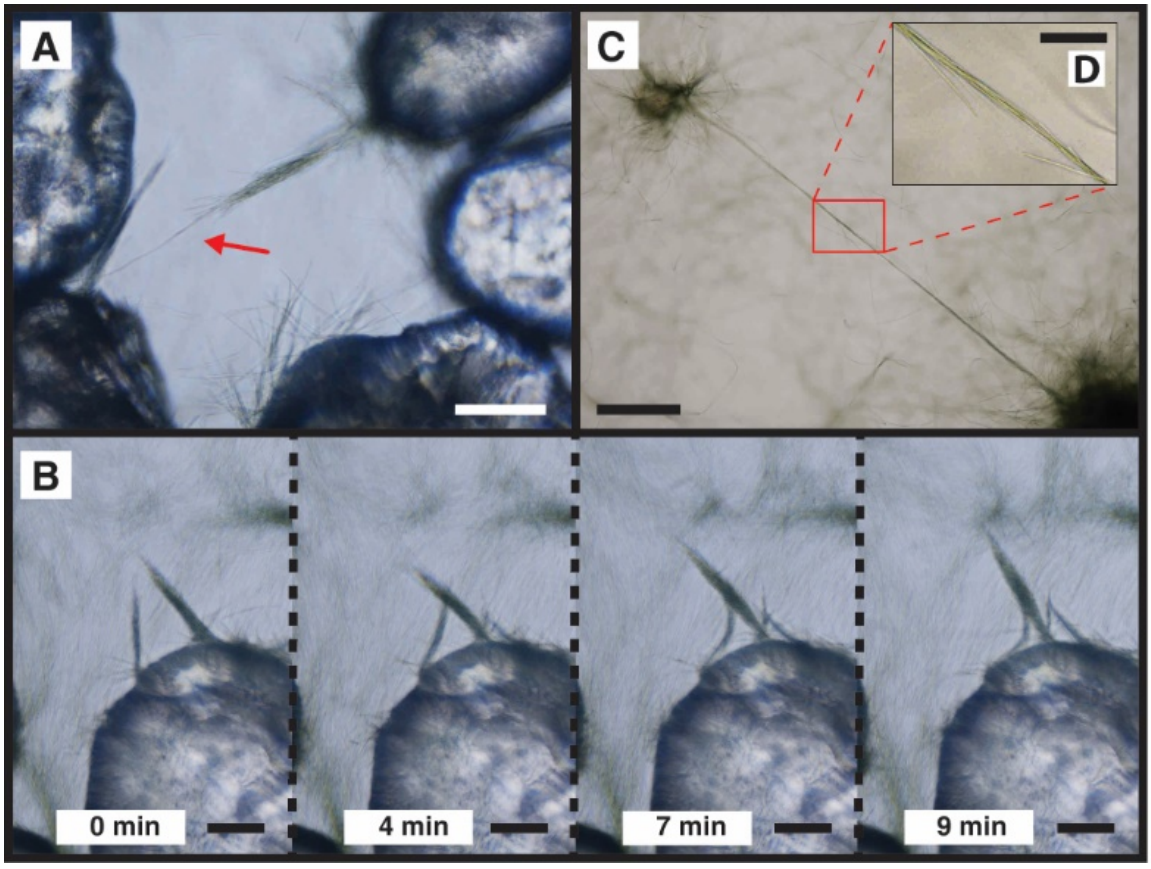

Figure 2.3. Microscopic views of filaments in tufts and star arms. (A) Tuft with extending filaments (arrow). Scale bar = 100 µm. (B) Merger of two tufts in time series. Scale bar = 100 µm. (C, D) Two star arms conjoined upon contact. Note that within the bridging arm, filaments have twisted around each other rather than contacting end-to-end. Scale bars = 100 µm (C) and 25 µm (D).

Figure 2.4. Formation of sand piles during cone formation. (A) Experimental cones showing individual sand piles under each cone. (B) Extended-depth-of-field, top-down view of sand piles after drying. (C) Sand grain spatial distribution analysis performed on B. Grid spacing = 200 μm. Red dot: original cone centers. Yellow outline: counted grain boundaries. Yellow line: distance of a grain center of mass to its closest cone center. Grid-based counting was employed to reduce selection bias. (D) Digital elevation model of the grain topography generated from B. (E) Linear regression analysis on the size distribution of the grains showing that larger grains are preferentially located near cone centers. Slope of the regression is significantly different from 0 (p(t) = 0.003). All scale bars = 3 mm.

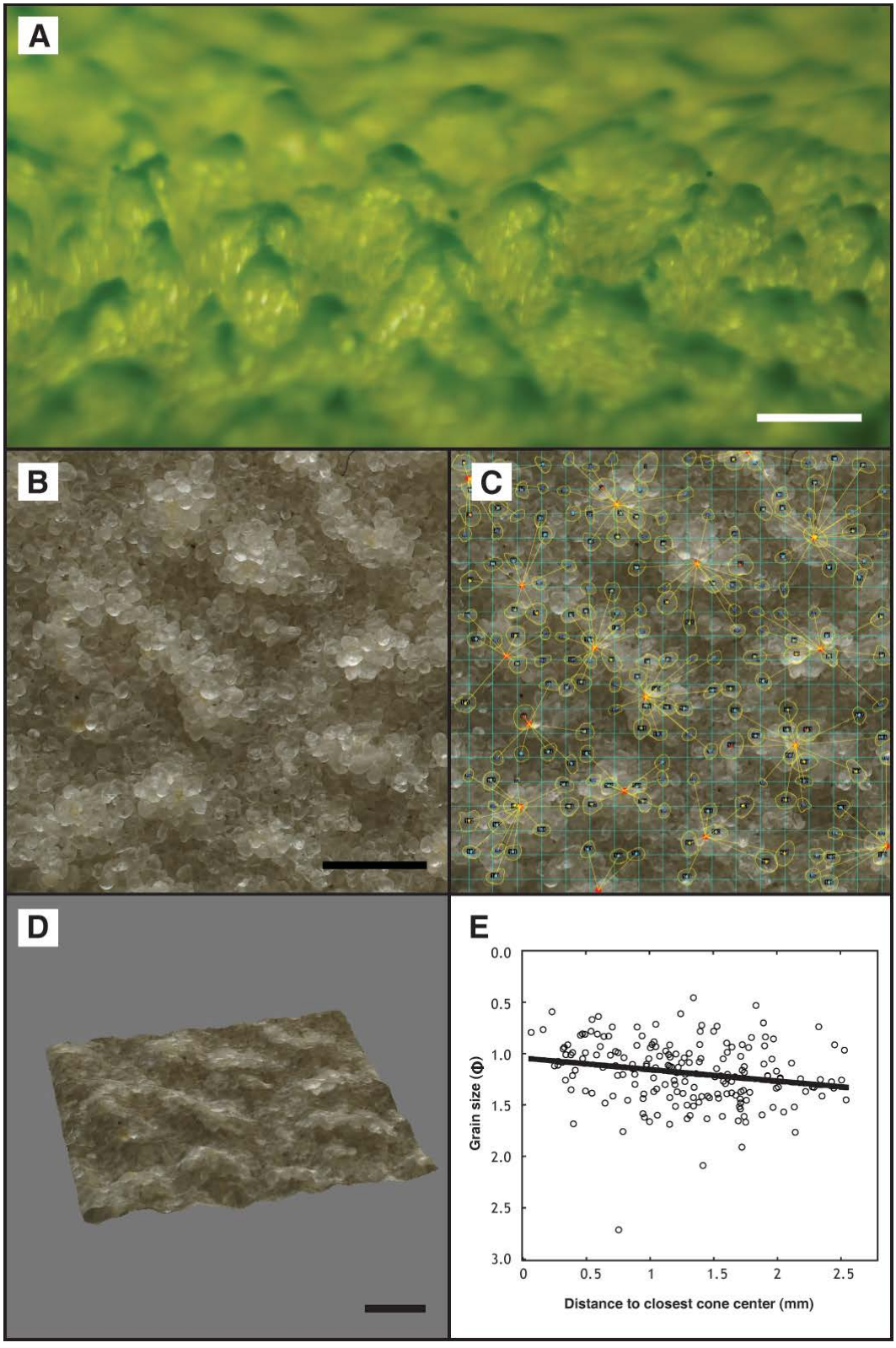
A
B
C
D
E
0.0
0.5
1.0
1.5
2.0
2.5
3.0
Grain size (Φ)
0
0.5
1
1.5
2
2.5
Distance to closest cone center (mm)

Figure 2.5. Sand sorting in Moodies Group (3.22 Ga) microbialites. (A) Symmetric mounds within crinkly laminated sandstone. Scale bar = 5 mm. (B) X-ray fluorescence map of the same region showing distribution of heavy minerals containing Ti (in green) and Zr (in red). Note that heavy minerals lie at the base of the mounds. Scale bar = 5 mm. (C) Enlarged mound under reflected cross-polarized light (high-resolution image stitched from a few dozen photomicrographs). Scale bar = 1 mm. (D) Normalized grain size distribution plot showing data from several symmetric mounds in different samples in Moodies Group sandstone. The analysis of the current sample is shown in solid black circles; those of other samples in solid grey. The grain sizes measured in our experiments are shown in open red circles. X-axis: normalized grain distance to cone-center (D) with respect to full cone-width at half-height maximum (FWHM). Y-axis: measured grain sizes (in ϕ scale) normalized to grains beyond the half-height maximum, where ϕ_0 is the mean grain size and σ_0 the sample standard deviation of the distribution (higher Y-axis value means larger grain size).

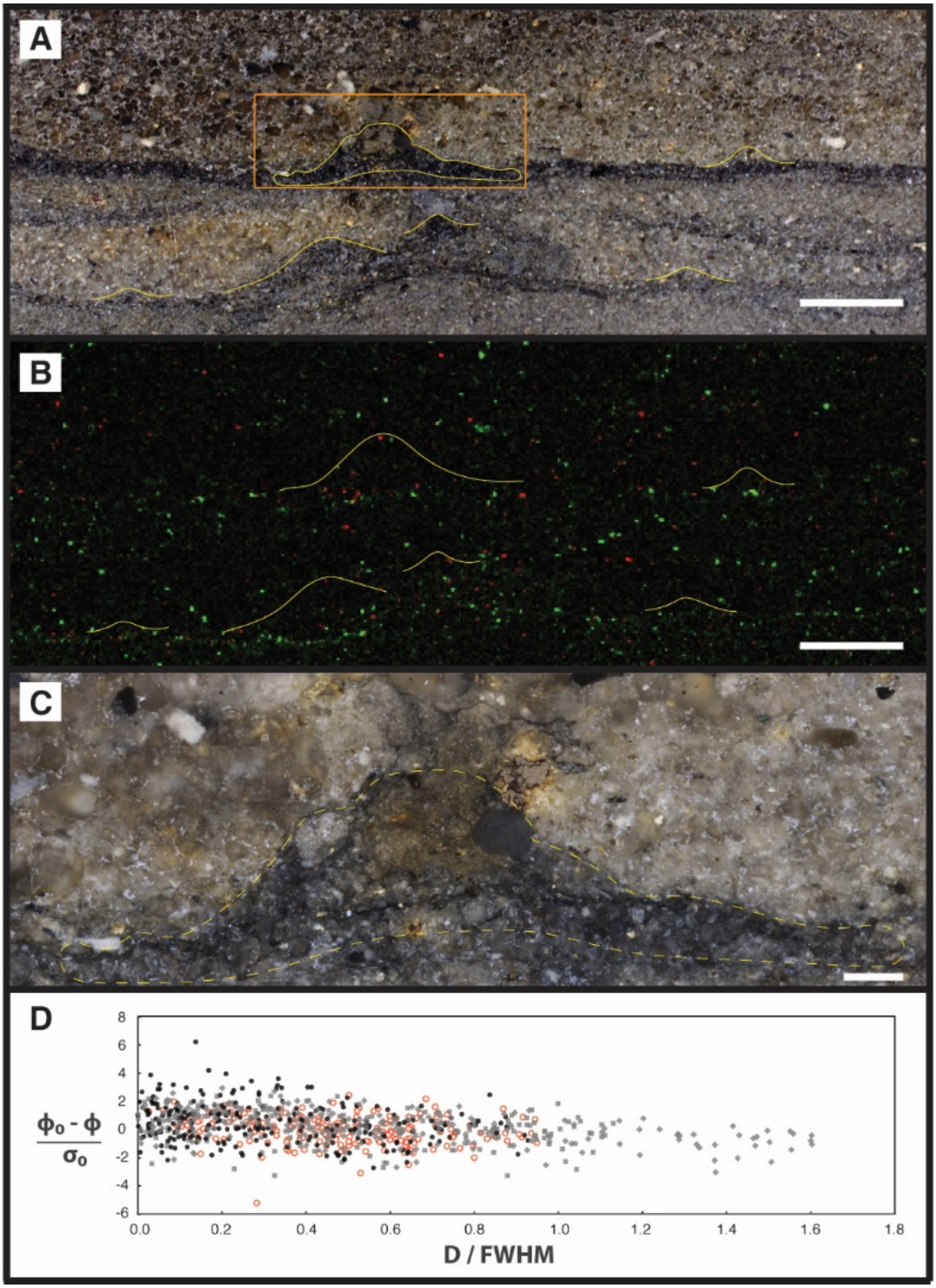
A
B
C
D
8
6
4
2
0
-2
-4
-6
0.0
0.2
0.4
0.6
0.8
1.0
1.2
1.4
1.6
1.8
D / FWHM
ϕ0 - ϕ
σ0

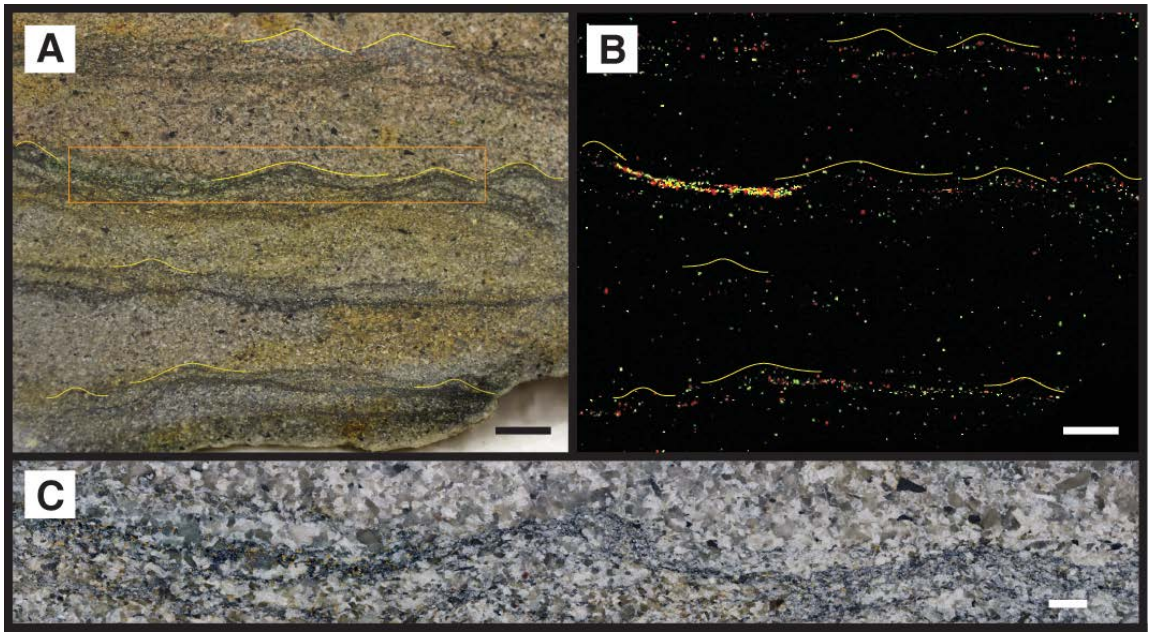

Figure 2.6. Sand sorting in a sample of Moodies Group (3.22 Ga-old) microbially laminated sandstone. (A) Cut and polished sample showing symmetric mounds within crinkly laminated sandstone. Scale bar = 5 mm. (B) X-ray fluorescence map of the same region showing distribution of heavy minerals containing Ti (green) and Zr (red) (overlapping grains may appear yellow). Note that heavy minerals concentrated near the bases of mounds. Scale bar = 5 mm. (C) Enlarged mound (rectangle region in A) under reflected cross-polarized light (high resolution image stitched from a few dozen photomicrographs). Grain point-count analysis was performed on this image by measuring grain sizes within and immediately below the dark lamina. Results are reported in the main text (Figure 2.5D). Scale bar = 1 mm.

Figure 2.7. Sand sorting in a sample of Moodies Group microbially laminated sandstone. (A) Cut and polished sample showing symmetric mounds within crinkly laminated sandstone (color-enhanced). Scale bar = 5 mm. (B) X-ray fluorescence map of the same region showing distribution of heavy minerals containing Ti (green) and Zr (red). Scale bar = 5 mm. (C) Enlarged mound (rectangle region in A) under reflected cross-polarized light (high-resolution image stitched from a few dozen photomicrographs). Yellow dashed region (within and immediately below the dark lamina) indicates where grain sizes were measured and counted. Results are reported in the main text (Figure 2.5D). Scale bar = 1 mm.

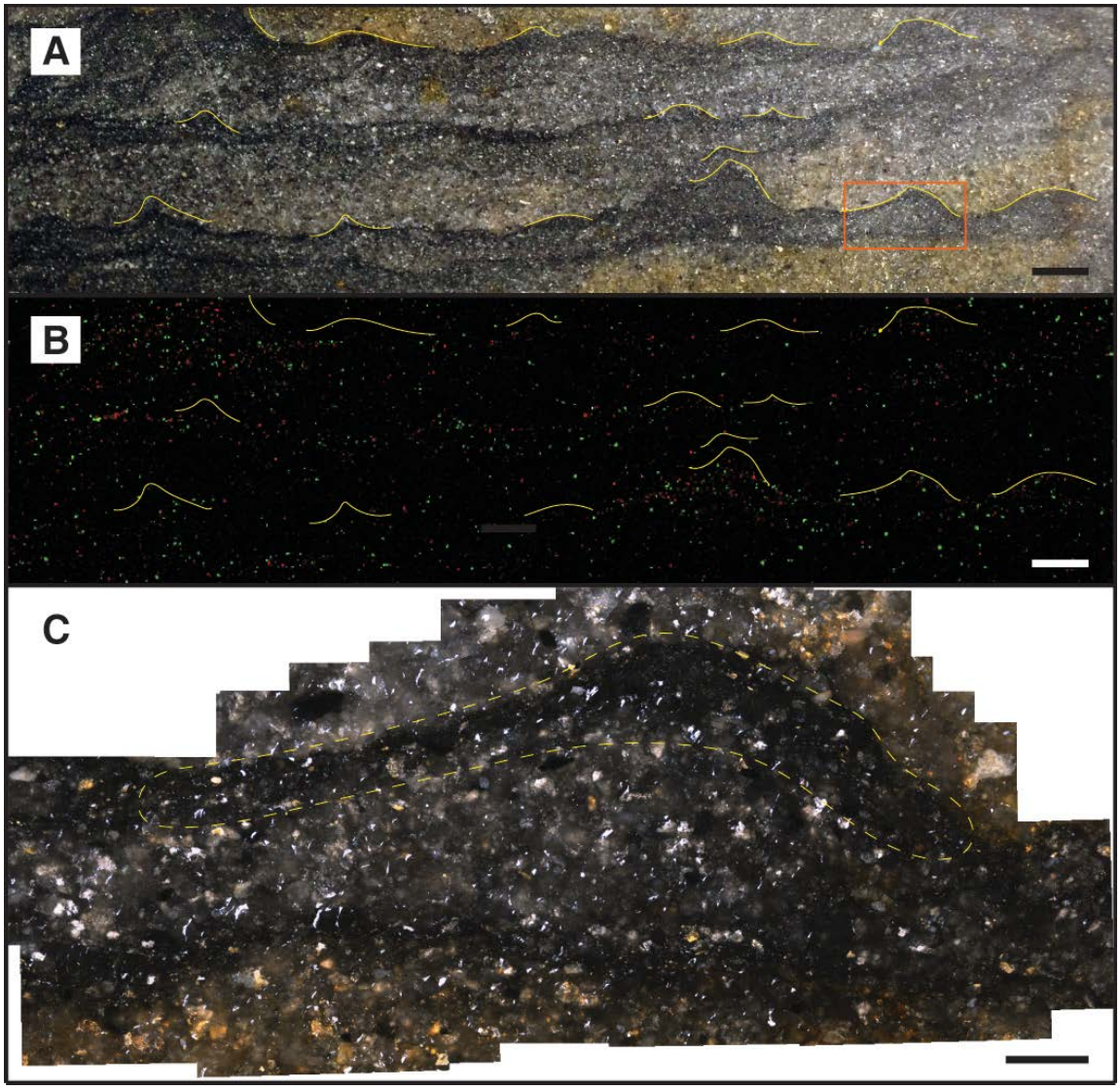
A
B
C

II.3.4 Videos

Videos are archived on a public data repository at figshare.com (Gong et al. 2015).

Link: Video 2.1

Video 2.1. Motion of early-stage cones on sand during the first week of incubation. Rapid motion toward the upper-left side of the frame through about 11:00 is due to lift-off of some cones from the sand base. Cone centers are 0.5-1.0 mm in diameter. [15-minute-interval time-lapse video encoded at 2 frames per second (fps)]

Link: Video 2.2

Video 2.2. Daily activities of cones as they became less mobile on sand at 2.5 weeks incubation. Cone with radiating arm structure is well-developed by 10:30-11:00, and disaggregation begins at 14:00 to 15:00. Cones are spaced on average 2 to 3 mm apart. [30-second-interval time-lapse video encoded at 10 fps]

Link: Video 2.3

Video 2.3. Activities of a single stable cone on sand after 3 weeks of incubation over one day and the following morning. Note twisting of tufts crowning the top of the cone during the day and partial unwinding by the next morning. The base of the cone is about 3 mm in diameter. [20-second-interval time-lapse video encoded at 18 fps]

Link: Video 2.4

Video 2.4. Behavior of eight-week-old mature cones covering sand surfaces. Cones

begin the day with crowning tufts arranged in loose, low-density heads. Within the first 30 minutes of illumination, heads contract and tufts wave and rotate, growing the underlying cones. The base of the mature cones are on average about 3 mm in diameter and spaced at about 3 to 5 mm apart. [30-second-interval time-lapse video encoded at 10 fps]

Link: Video 2.5

Video 2.5. Merging of two cone centers on smooth agar surface. Note that the region immediately around the cones has been swept clear of tufts. The size of the final merged cone is about 1.5 mm in diameter. [30-second-interval time-lapse video encoded at 10 fps]

Link: Video 2.6

Video 2.6. Streaming of *Leptolyngbya* culture on smooth agar surface. Note travelling density waves along streams. Waves travel faster than individual bacteria. Streams are 100-200 µm wide. [5-second-interval time-lapse video encoded at 30 fps]

Link: Video 2.7

Video 2.7. Sand grain rolled by merging cones. Note that the sand grain rolls towards the cone on the left starting when the two cones connect through radiating arms. Sand grains are between 200-400 µm in diameter. [30-second-interval time-lapse video encoded at 8 fps]

II.4 CONCLUSIONS

The formation of cones likely increases the diffusive exchange between the mat community and the overlying fluid in stagnant environments (A. P. Petroff et al. 2010). Our results suggest that *Leptolyngbya* filaments achieve this result despite growth on topographically heterogeneous sediment surfaces by coordinating group motion in a sticky random walk that mimics diffusion, producing structures with sizes proportional to diffusive length scales. Coordinated taxis in a biofilm is a key mechanism of bacterial multicellularity (Lyons & Kolter 2015) capable of achieving benefits for the population as a whole. Evidence of this behavior in 3.22 Ga-old microbial mats therefore provides a new record of multicellular organization of some of the earliest life on Earth.

II.5 METHODS

II.5.1 Culture Conditions

Leptolyngbya was cultured on quartz sand (Videos: 2.1-2.4, 2.7) and on smooth 1% agar surface (Videos: 2.5-2.6). Sands (VWR: Macron) was triple acid-washed and DI-water washed multiple times to remove trace metal contaminants. All cultures were submerged under 1 cm of stagnant TES-buffered BG-11 medium (Castenholz 1988) at 42 °C with regular 12-hour day-night cycles.

II.5.2 Videos

Microscopic time-lapse movies were produced by taking software-automated (Lundvall 2013) microscopic images at set intervals, which were then encoded into

movies (The MPlayer Team 2000). Portable but high resolution 5 Megapixel USB microscopes (Adafruit® Industries, Inc.) with manually adjusted optical elements (to allow sharper images at specific distances) were used to take images without disturbing the growth of the mats in situ.

II.5.3 Sand Sorting Experiment and Analysis

After five to six weeks of cone growth, small sand piles became visible underneath biological cones (Figure 2.4A). In a control experiment, an abiotic culture was prepared using the same initial flat sand surface in which no bacteria were inoculated. This sand surface remained flat throughout all treatments. For quantitative grain analysis, liquid media were carefully removed by pipette and the remaining microbial mat and sand were air-dried at room temperature for one month. Images were compared to ensure that the drying process did not affect the sand surface topography. After one month, most of the mat had lost its bright green chlorophyll pigmentation and appeared translucent brownish-yellow, leaving the underlying sand grains visible. The original conical mat tips were still identifiable because they were biomass-dense relative to the rest of the mat and therefore slightly darker brown in color (Figure 2.4B).

An extended-depth-of-field technique was used to image cone piles by taking approximately 40 consecutive images at heights above the sand bed varying by 50 µm steps. Images were recombined using an ImageJ plug-in (Forster et al. 2004; Aguet et al. 2008; Schneider et al. 2012; Schindelin et al. 2012) to produce a final image in which all grains were in focus (Figure 2.4B). A robotic Z-axis was built in order to achieve the

necessary positional accuracy (<2 μm) for the camera (Pentax DSLR K5 with 35 mm macro lens). This method ensured that (a) no spurious grain size variations were produced due to varying grain distance from the camera, because the camera itself was moved and only the in-focus portion of the image was incorporated into the final combined image; (b) all grains were sharply focused despite their locations on varying topography; and (c) digital elevation models of the mound surfaces were also obtained (Figure 2.4D). Grain point-counts using well-established methods (Chayes 1956) were performed digitally with a 200 μm-spacing grid in ImageJ. To minimize selection bias, only recognizable grains that fell on the grid's intersections were measured. Because the quartz grains were slightly transparent, it was possible to see through a grain and therefore have overlap with another. Only grains completely exposed in more than half of their cross sections were counted, with the other half estimated through the overlying grains. Grain boundaries were traced by hand and grain sizes were estimated as $2 \cdot \sqrt{A/\pi}$ where A is the cross-sectional area. Each grain position was located using the center of mass of the enclosed area, and the distance to the nearest cone center was calculated (Figure 2.4C). Finally, regression analyses were performed to test for relationship between grain size and distance to the closest cone center (Figure 2.4D). Because grain sizes were log-normally distributed, all calculations were performed in ϕ units, where $\phi = -\log_2(D)$ and D is the grain diameter in mm. This transformation is standard in the statistical analysis of grain size distributions.

II.5.4 Moodies Group Sandstone Grain Analysis

Slabs of Moodies Group sandstone samples were first cut serially into 1 to 3 mm-thick slices perpendicular to bedding. By comparing the shapes of cones between consecutive slices, most cones were found to be radially symmetric. For grain measurement and counting, slabs were machine-polished to 3000 grit. A digital grain-count procedure was performed by first digitally stitching high-resolution (400×) photomicrographs collected under cross-polarized episcopic illumination (Nikon Eclipse LV100POL petrographic microscope, Adobe Photoshop CS5). The stitched image was imported to ImageJ and overlain by a 200 μm grid. Grain size estimation and testing for size sorting proceeded as for experimental sand fields. For the analysis of mineral distributions, X-ray fluorescence (XRF) scans were performed at a resolution of 100 μm per pixel (Horiba XGT7000 μXRF Analyzer, 50 kV accelerating voltage, 1 mA current). Because zircon ($ZrSiO_4$) and rutile/anatase (TiO_2) grains were abundant in these rocks, heavy mineral distributions were visualized by preparing false-color images of Zr $K_{\alpha 1}$ and Ti $K_{\alpha 1}$ integrated fluorescence counts (Figure 2.5B).

CHAPTER III

FORMATION OF MICROBIAL STREAMERS BY SHEAR-INDUCED VISCOPLASTIC DEFORMATION AND THE EFFECTS ON FLOW STRUCTURE

III.1 OVERVIEW

Microbial streamers are elements of surface-attached microbial communities that paradoxically seem to roughen mats under rapid, high shear flows, potentially exposing the mat to greater risk of erosion. These are common microbial structures formed in moving waters, yet the mechanism of their formation and effects on mat erosion are poorly understood. We test a model that streamers are produced by shear-induced viscoplastic deformation, and they form passively but ultimately act to heal detached boundary layers. Consequently, the presence of streamers helps smooth the bedding surface hydraulically while diverging shear stress for basal mats. Numerical models as well as laboratory flume experiments were developed to gain quantitative insights on the structure of flows around small projections on surfaces. Results show that boundary layer separation caused by sufficient shear induces localized deformations at the top of the projection, ultimately initiating streamer formation. With insufficient surface relief, streamers are unable to rise up from basal mats. Thus, a combination of sufficient topographic relief and flow strength is required for streamer formation. In addition, flow structure analysis indicates that the presence of streamers on the top of surface projections reduces separation bubbles as well as shear stress at the base, thereby making the surface hydraulically smoother. These results suggest a novel set of feedbacks that

reduce net mat erosion in energetic flows, and provide insights into the evaluation of biosignatures in sedimentary rocks deposited in the presence of microbial mats in moving fluids.

III.2 INTRODUCTION

Microbial streamers are common and fascinating expressions of microbial growth in rapidly moving fluids that generally stem from surface-attached microbial mats with elongated, flexible bodies oscillating in the downstream bulk fluid. Streamers frequently form in rivers (Hall-Stoodley et al. 2004), acid-mine drainages (Edwards et al. 2000; Kay et al. 2013), hot-springs (Reysenbach & Cady 2001) as well as in industrial (Picologlou et al. 1980) and clinical (Parsek & Singh 2003) environments. Streamer structure may result a unique fossil record when mineralized quickly (Flot & Cady 2002; Reysenbach & Cady 2001); however in most modern environments the preservation potential is low, because streamer bodies either get eroded too quickly before mineralization or settle down when flow decreases, merging back to surface microbial mats. Despite being a transient mode of growth, streamers prevail in rapid flowing environments as dominant and resilient microbial structures. It remains unclear how natural streamers initiate in high shear flows and why they are the preferred mode of growth in these environments.

Hydrodynamically, it is well-established that forming a streamlined body in moving fluids has the benefit of reducing drag (Vogel 1994; Stoodley et al. 1998). However, it is less well understood how changes in flow structure caused by complex

geometries affect shear on surfaces. As a result, most of these problems must be dealt with numerically and experimentally. There are two general mechanisms that describe how drag was produced, both related to the internal viscous effects of the fluid: *skin friction* and *form drag* (Vogel 1994). Although both contribute to the overall drag at all flow regimes, skin friction is mainly caused by the no-slip condition of the fluid at the material surface and is more apparent in viscous, laminar flows. As the flow transitions to be more turbulent, form drag rises quickly and dominates (Vogel 1994). For example, when estimating the overall drag of a circular cylinder in different flowing medium, Vogel (Vogel 1994) showed that the form drag constitutes 57% at *Re*=10; 71% at *Re*=100; 87% at *Re*=1000; and 97% at *Re*=10,000, where Reynolds number is defined as $Re = ud/\nu$, u the velocity, d a characteristic length scale and ν the kinematic viscosity. In hotspring open channel flows where many natural streamers form, at average flow speeds between 1 - 100 cm s^{-1} and hydraulic radius 1 – 10 cm, *Re* of the bulk flow can range from 100 - 100,000. Although the *Re* in different flow geometries is not always directly comparable, the fact that both open channel flow and the flow around a circular cylinder would transition to turbulence around *Re*=500-4000 suggests that in these environments, form drag likely represented a significant contribution. Form drag is produced mainly due to changes in flow structure and the fact that energy is invested accelerating the fluid around obstructions, yet it is not returned to the system but dissipated as downstream wakes and eventually to heat. Unlike skin friction which scales to total surface area, form drag is highly dependent on, and sensitive to, the shape, rigidity and orientation of the body in the flow (Vogel 1994).

Obtaining details on flow structure is key to understand the hydrodynamics of developed streamers, but because streamers are also evolving structures, it remains unclear how and under what conditions streamers may initiate in shearing flows next to a surface. On the contrary, given an erosive turbulent flow with thin boundary layers shaping a smoothly-grown mat, it seems paradoxical that any streamer structure could form at all (Tice et al. 2011; Tanja Bosak 2012). Interestingly, streamers are not limited to turbulent flows. Rusconi *et al.* (Rusconi et al. 2010; Rusconi et al. 2011) reported that streamers may commonly form in laminar-flow, microfluidic devices through angled corners and bends. They concluded that secondary flows (redirected flows behind projections) are the mechanism inducing streamer formation (Rusconi et al. 2011). Recently, similar observations were noted when designing and testing microfluidic filters: streamers are much more prominent in staggered channels in comparison to straight channels (Marty et al. 2012). Both studies provided additional insights into where streamers are likely to form in laminar flows, yet it is still difficult to infer from these studies the conditions required for streamer initialization in natural environments.

We test the hypothesis that in addition to growth structures, streamers could also behave like a type of Bingham fluid composed of viscoelastic microbial communities. Under fluid shear, the materials are being reshaped slowly but continuously. The model requires a thin biofilm to first initialize on existing surfaces. Then, it is deformed by shearing fluids into a streamer-like shape. Since most environmental flows have turbulent boundary layers thicker (~100 μm) than one individual microbe (1-2 μm) (Jørgensen 1994), this boundary layer provides enough space and protection for biofilm

to initially grow in most flowing environments.

III.3 RESULTS AND DISCUSSION

III.3.1 Field Observations

In order to characterize how streamers occur in modern natural environments, we surveyed modern hot-spring outflow channels and found that streamers are most often found in shallow, channelized, surface flow systems, suggesting that these microbial features require a sufficiently high flow strength to form, but once established, are well adapted to strong fluid shears (Figure 3.1). In these environments, centimeter to decimeter scale bundles or sheets of communities composed of dominantly filamentous organisms were found utilizing photosynthesis or chemosynthesis. Qualitative observations in open-channel-flow microbial streamers in modern hotsprings indicate that (1) they are dynamic features flapping along with the turbulent flow; (2) A non-random spacing and length are often established among streamer bodies in fixed flow conditions; (3) They frequently initialize from local topographical highs; (4) Bundles, feathers and sheets of microbial filaments are the typical streamer morphology; (5) Different microbial metabolisms and communities produce varied streamer morphologies in similar flow conditions. These observations hint that a complex suite of environmental and biological factors are at work influencing the growth and physical characteristics of streamers.

III.3.2 Initialization of Streamers

To investigate how streamers initiate from locally rough surfaces under fluid shear, we constructed a simple 2D fluid-structure interaction model using open source C++ finite element library deal.II (Bangerth et al. 2015; Bangerth et al. 2007). The model assumed that the fluid flow is laminar, and a thin biofilm residing on a local roughness element behaves like a soft elastic solid, deforming according to the fluid stress until an equilibrium is reached (Appendix A4). By using realistic physical parameters and consecutively deforming the finite element meshes, slow plastic flow of the biofilm can be simulated (Video 3.1). This model demonstrates that even with laminar flows, higher fluid velocity at the top of the roughness element translates to a local lift force that deforms the biofilm upwards into the flow, driving the initialization of a streamer (Figure 3.2). Although this model assumed laminar flows, turbulent flows often drives a steeper vertical velocity gradient; therefore an analogous mechanism may be in place providing lift.

To examine the effects of turbulence on streamer initialization, we observed the turbulent flow structure experimentally around a rigid local roughness element (hemisphere) in a linear flow flume, where flows can be visualized with neutrally buoyant tracer particles illuminated by a sheet laser (see Appendix A5 for the linear flume design and construction). With videos taken from high speed cameras at 240 frames per second (Video 3.2), quantitative information was extracted in MATLAB using Particle Image Velocimetry (PIV) (Thielicke & Stamhuis 2014) and Particle Tracking Velocimetry (PTV) (Brevis et al. 2010) programs. Results show that the

presence of a surface-attached local projection in the turbulent flow induced boundary layer separation with a well-defined separation bubble (Figure 3.3B). The backflow behind the projection was significant, which caused fluid shear to localize towards the top of the projection (Figure 3.3C). The projection top was also the site of higher mixing (Figure 3.3D) and focusing secondary flows in 3D (Figure 3.3E and F), all of which were likely to confine shear at the projection top. If a layer of biofilm is present on the surface, it would be expected to deform from the top of the projection and extend into the shearing fluid.

In order to verify that streamer-like structures can initiate from local projections, we replaced the hard plastic material in the previous experiment with a viscoelastic gel material made from 1% Xanthan Gum, mimicking the material properties of microbial EPS, while keeping the physical dimensions and flow conditions the same. Indeed, with the help of time-lapse video the formation of a streamer-like body is observed in 3-4 hours (Video 3.3). Significantly, this experiment showed that streamer formation is a continuous process in which deformation happens at a faster rate along EPS-fluid interfaces. In addition, it demonstrated that the viscoelastic material property of an EPS material is key to evolving streamer shapes. Since the deformation process is viscoplastic rather than truly viscoelastic (which implies reversibility), irreversible elastic (brittle) as well as microscopic plastic failures are common features during the deformation process and are documented in the video as well. This observation also indicates that during the formation of streamers, cellular biomass is constantly being sheared off from the streamer-fluid interface into the moving fluid, thus making

streamers a constant but resilient source for biomass dispersal. In addition, because streamers interact directly with turbulent flow, their biological growth is thus not as limited by diffusive transport as the microbial mat community immediately adjacent to surfaces. This makes the streamer community a potentially more productive microbial ecosystem.

To finally observe how realistic streamers may initiate from filamentous bacterial communities, we performed growth and erosion experiments inside a circular shear flow reactor (see Appendix A6 for the reactor design). Results show that streamers preferentially initiated from the top of localized mat projections (Video 3.4) as expected and that the formation happened in a duration from just a few minutes to an hour, much faster than the doubling time of the organism (on the order of 8-12 hours, data not shown). This observation indicates that deformation likely plays a more prominent role in forming streamers than growth at the beginning of streamer formation. However, given that streamer communities are not likely limited by nutrition or space, ignoring erosion, the growth rate of the community can be modeled to depend on the population size, P and a constant growth rate factor r, so $\partial P/\partial t = r \cdot P$, which results in $P(t) = P_0 \cdot e^{r \cdot t}$, the classical exponential growth equation. Because the growth rate is not a constant but increases as the population expends, there exist a time when the rate of growth will catch up with the rate of erosion, establishing an equilibrium between the two processes, finally resulting a characteristic streamer morphology.

III.3.3 Hydrodynamic Effects of Streamers

In order to examine the fluid structure around a single streamer in the presence of a field of streamers, we visualized the moving fluid around one artificial streamer made from a cotton string by filming across several parallel and vertical sheet laser planes parallel to the flow direction (Video 3.4 and Figure 3.4A). Velocity vectors derived from PIV computation were averaged over 2 seconds at 240 FPS (480 frames). This technique revealed the mean 3D flow structure around the streamer (Figure 3.4B). Direct comparison shows that the presence of streamers reduced the size of the separation bubble by about a factor of 2 (Figure 3.5). By reducing boundary layer separations, which can be seen visually from the velocity distributions (Figure 3.4B), fluid structure is hydraulically smoother by definition.

A qualitative fluid drag reasoning suggests that in unidirectional, transitional to turbulent flows, an elongated streamer body is expected to amplify skin friction due to increased surface area, but reduce form drag even more by decreasing boundary layer separation and downstream wakes, thereby providing a mechanism to reduce the overall drag of the surface. However, this result is likely only valid for short or rigid streamers. Although direct drag measurements were not performed in this research, it is expected that as flexible streamers grow longer and oscillate in the bulk fluid, form drag may increase again due to oscillation-induced flow separation and creation of downstream wakes (Taherzadeh et al. 2012). This effect may eventually counter the benefit of having a streamlined body (Stoodley et al. 1998). Alternatively, streamers may join together to form larger scale sheets or feather-like shapes, improving rigidity while reducing

oscillation. These morphologies are commonly observed in hotspring streamers forming in channel flows (Figure 3.1D).

III.3.4 Figures

Figure 3.1. Varieties of microbial streamer morphotypes found in natural environments. (A) Streamers found in Stinking Springs (Utah, USA) hotspring composed of primarily filamentous cyanobacterium *Leptolyngbya* sp. with a white-color core consisting of pure elemental sulfur precipitated chemically from the bulk fluid. Flow direction is to the left of the picture. (B) Streamers found also in Stinking Springs (Utah, USA) hotspring (downstream from A), consisting of certain unknown white-colored filamentous bacteria likely utilizing sulfate reduction as their energy source. Flow direction is from bottom to the top. (C) Streamers in Yellowstone National Park found in hotspring outflow channels (flow direction is to the right). Note that bundles of filamentous cyanobacteria form preferentially behind local projections downstream. (D) Feather-like Yellowstone National Park streamers growing in a hotspring outflow channel at a temperature of around 60°C. Flow direction is to the right in the picture. All scale bars = 3 cm.

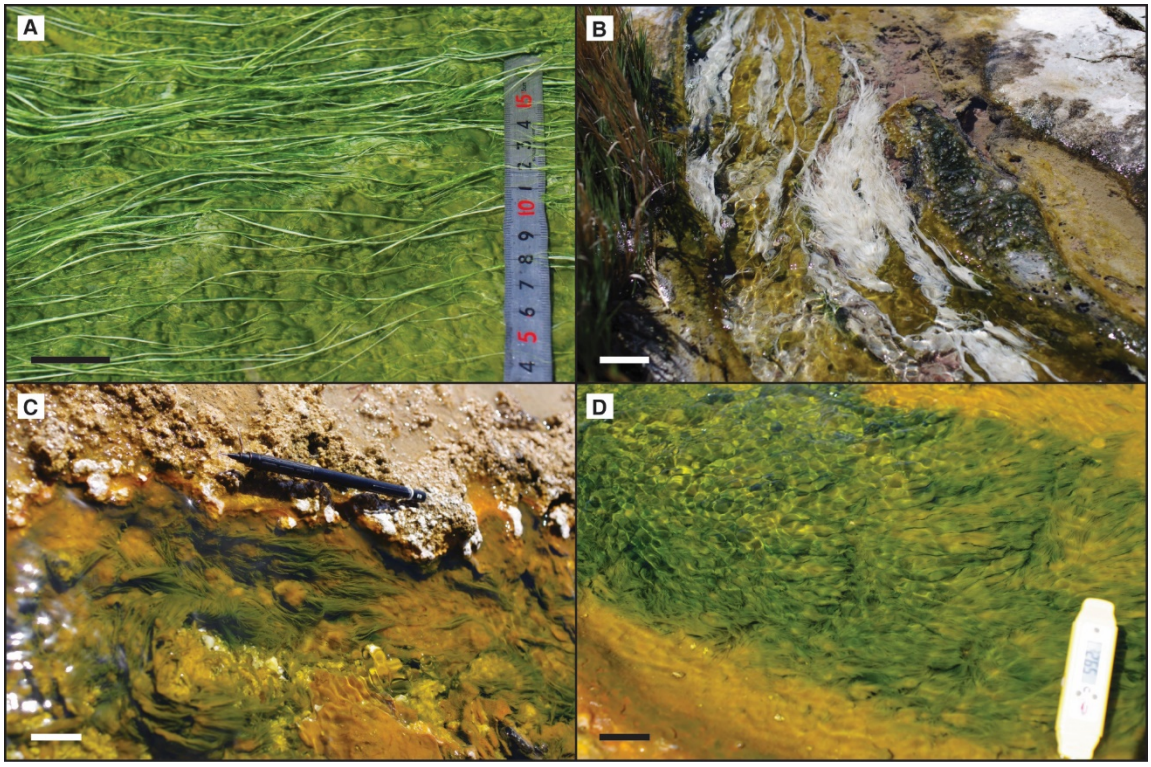
A
B
C
D

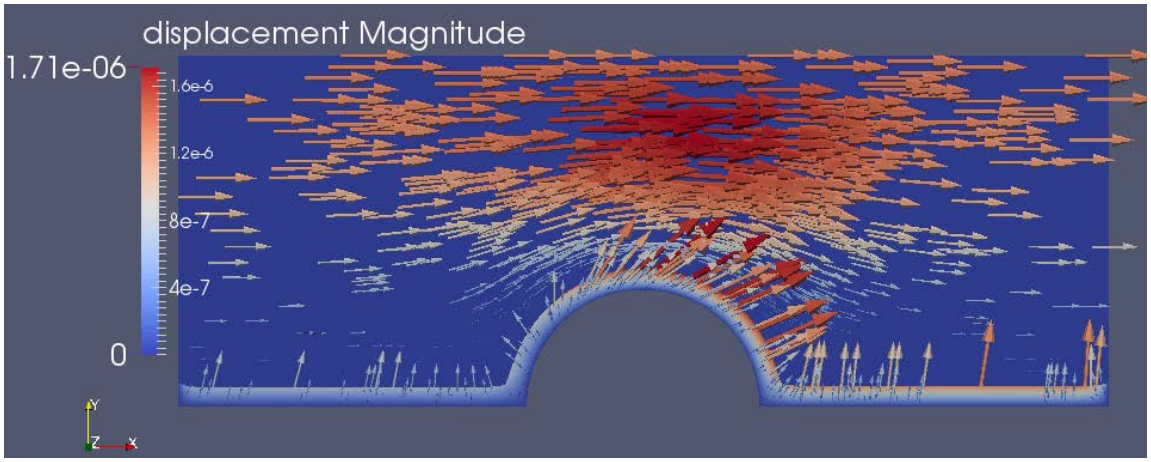

Figure 3.2. 2D finite element calculation of fluid stress around a thin biofilm residing on a local roughness element (a semicircle). The scale bar denotes the scale of elastic deformation of the biofilm. Arrows in the fluid domain are velocity vectors of the fluid. Arrows in the solid domain are deformation vectors of the biofilm induced by the fluid. Physical parameters: thickness of the biofilm is 0.5 mm, fluid domain height 7 mm, fluid domain width 20 mm. Viscosity of water is 0.894×10^{-3} Pa·s. Elasticity of biofilm, $\lambda=\mu=50$ Pa (Lame's first and second parameter). Top boundary fluid speed is 10 cm·s^{-1}. For more details on the numerical model see Appendix A4.

Figure 3.3. Mean turbulent flow structure around a local projection (hemisphere with diameter 1 cm) visualized by PIV. Flow direction is from left to right with speed 20 cm/s. High speed images were taken at 240 frames per second (FPS) and averaged over 3 seconds. (A) Snapshot of experiment video. (B) Colored velocity magnitude profile (blue to yellow colors indicate flow speed from low to high). Velocity vectors are also plotted (same in all images). Note the appearance of the separation bubble behind the project (indicated by arrow). (C) Shear rate profile (blue to yellow colors indicate fluid shear form low to high). Note shear is high near the top of the projection. (D) Vorticity profile (blue to yellow colors indicate vorticity from negative [counter-clockwise] to positive [clockwise]. Vorticity describes mixing effect of the flow. (E) Divergence profile (blue to yellow colors indicate negative [local drain] to positive [local source], respectively of the flowing particles). Divergence describes locally how flow goes into and out of the 2D plane, as an indirect measure of mixing and general flow direction in 3D. (F) Line integral convolution profile. Line integral convolution is a technique to visualize complex fluid paths (Cabral & Leedom 1993), an excellent tool to visualize separation bubbles, as indicated by the arrow.

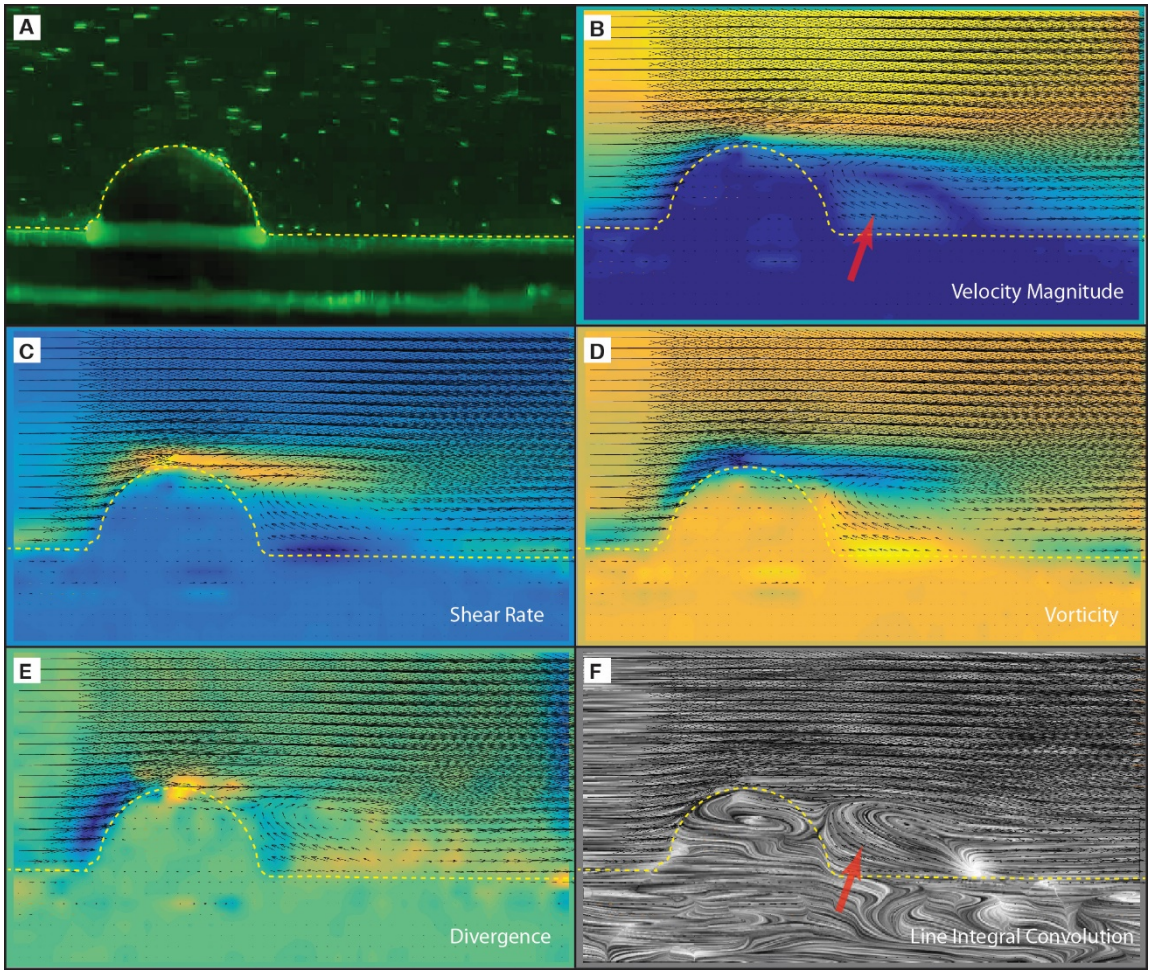
A
B
Velocity Magnitude
C
Shear Rate
D
Vorticity
E
Divergence
F
Line Integral Convolution

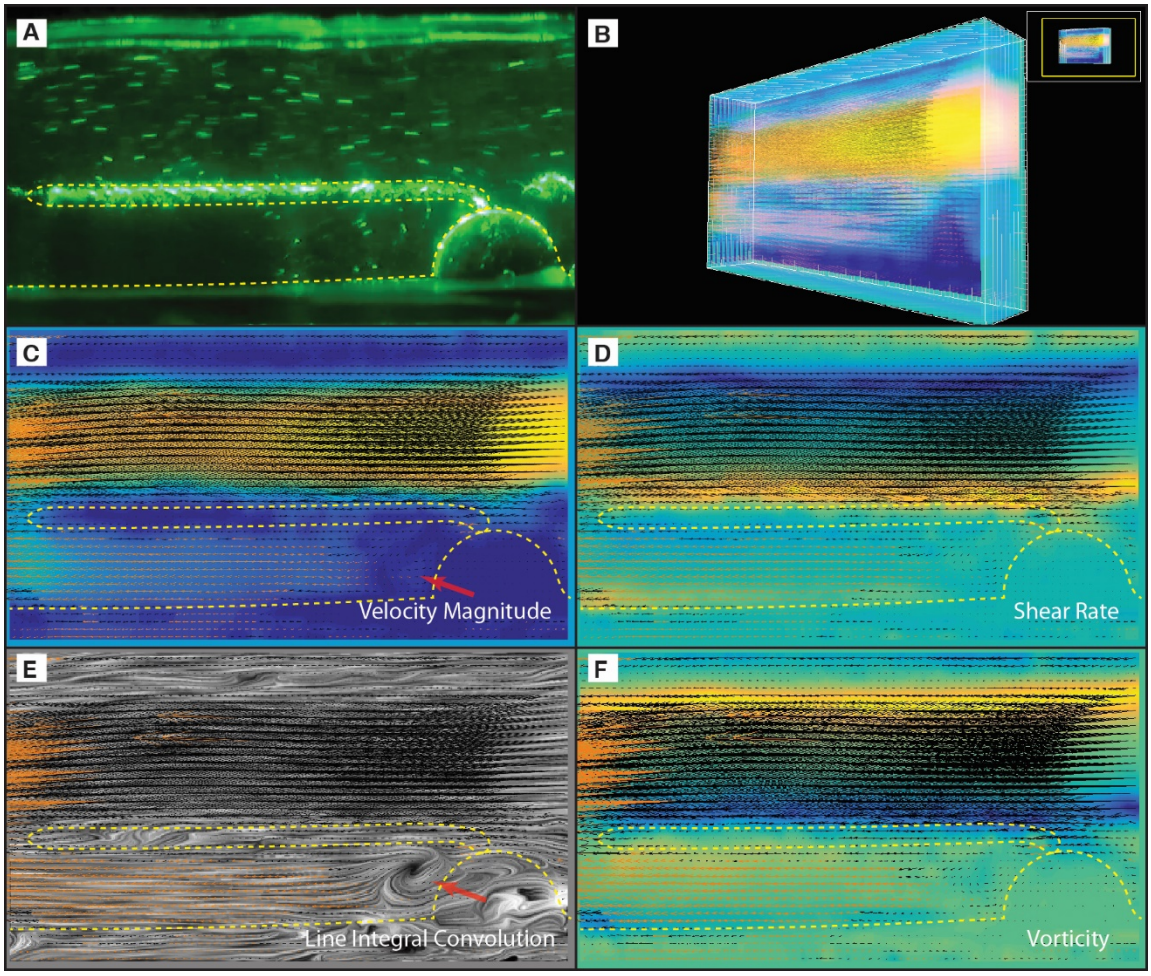

Figure 3.4. Mean turbulent flow structure around the same local projection with an artificial streamer attached, visualized by PIV. Streamer is about 3mm thick in diameter. Flow direction is from the right to the left at about 20 cm/s. (A) Snapshot of experiment video. (B) 3D mean turbulent velocity profile reconstructed with 5 consecutive vertical laser sheets 2mm apart across the streamer body (measured separately and recombined). (C) Velocity magnitude profile at the center of the streamer body. (D) Simple shear rate profile at the center of the streamer body. (E) Line integral convolution profile at the center of the streamer body. Arrow indicates the separation bubble. (F) Vorticity profile.

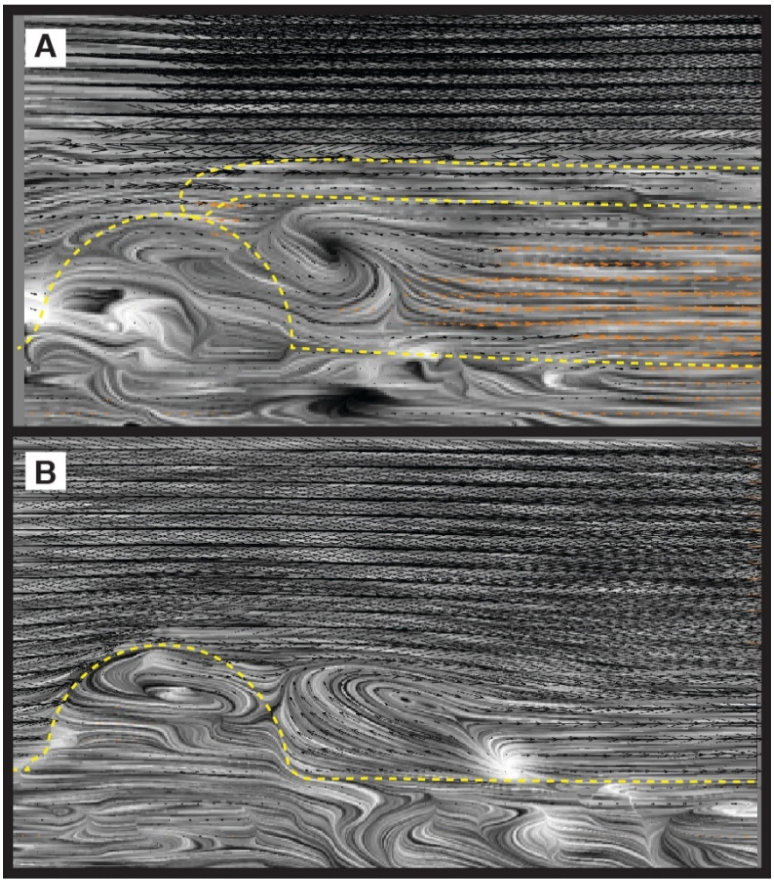

Figure 3.5. Direct comparison of the size of separation bubbles behind objects. (A) A semi-sphere with a streamer attached on top. (B) The same semi-sphere without a streamer. Flow speed is the same in both scenarios at about 20 cm per second. The semi-sphere has a diameter of 1 cm. There streamer is about 1 mm thick.

III.3.5 Videos

Videos are archived on a public data repository at figshare.com.

Link: Video 3.1

Video 3.1. Finite Element simulation of successive deformation of an elastic solid film (0.5 mm thin, representative of a realistic biofilm) resting on a semi-circular local projection. Arrows in the fluid domain are velocity vectors sampled at randomly chosen points. Arrows in the solid domain represent elastic deformation of the solid. Detailed description and parameters of the model are summarized in Appendix A4.

Link: Video 3.2

Video 3.2. Raw slow motion video (240 frames-per-second) of the flow structure around a local semi-spherical projection at flow speed of about 20 cm per second in a linear flume. Flow direction is from left to right. The spherical projection has a diameter of 1 cm. Neutrally-buoyant seeding particles of sufficient quantity are excited by a sheet laser from above, which is then used for quantitative PIV flow analysis (Figure 3.3).

Link: Video 3.3

Video 3.3. Deformation of a soft gel matrix made of 1% Xanthan Gum resembling the material property of bacterial EPS. The matrix is attached to the surface via a circular patch of Velcro (diameter 1 cm). Deformation was analyzed by taking a time-lapse video for a duration of about 7 hours. A stream-like flexible structure was formed in 3-4 hours.

Link: Video 3.4

Video 3.4. Formation of cyanobacterial streamers from small chunks of microbial mats during shearing flow in a circular flow reactor. Small streamers initiated within 20 minutes from the top of the mat chunks, indicating deformation rather than growth is the main mechanism at inducing streamer formation. Mat chunks are from 1-3 mm large. Flow speed is roughly 2-4 cm per second.

Link: Video 3.5

Video 3.5. Raw slow motion video (240 frames-per-second) of the flow structure around a local semi-spherical projection at flow speed of about 20 cm per second in a linear flume. An artificial streamer made of a cotton string is attached at the top of the projection. The diameter of the cotton string is about 1 mm. Flow direction is from right to left. The semi-spherical projection has a diameter of 1 cm. Neutrally-buoyant seeding particles are excited by a sheet laser from above, which is then used for quantitative PIV flow analysis (Figure 3.4).

III.4 CONCLUSIONS

Microbial streamers are adaptive structures easily deformed due to surface-attached microbial mats being sheared by moving fluids. Deformation at the top of existing surface roughness ultimately initiates as extended flexible structures flapping in the moving fluid. In this process, the microbial mat behaves like a Bingham fluid, deforming slowly but continuously. Both laminar and turbulent flows, with sufficient surface fluid shear and topological relief, can induce the formation of streamers. Hydrodynamically, the presence of a field of streamers self-organizes and reattaches broken boundary layers, thereby reducing the shear stress experienced in basal mats. Formation of streamers may be a common mechanism by which microbial mats withstand high shear flows, although it is most predominantly found in unidirectional, high shear turbulent flows in natural environments.

III.5 METHODS

Linear and circular flow flumes were designed and built to investigate the effect of hydrodynamics on surface roughness structures (see Appendix A5 and A6 for the design and construction). Neutrally-buoyant tracer particles were added to the fluid first, then a custom-mounted pulsed laser sheet was used to illuminate any 2D slice of the flow structure in any direction. Videos of moving tracer particles perpendicular to the viewing direction were recorded with a high speed camera (JVC GC-PX100B) at 240 frames per second. With this technique, quantitative information can be extracted using PIV and PTV programs developed in MATLAB (based on open source projects PIVlab

and PTVlab).

Artificial EPS gel material was formulated by hydrating Xanthan Gum (Sigma Aldrich) to a final concentration of about 1% with water, which was then impregnated with a small amount of tracer particles. After adequate mixing, the gel-forming step took place in a 4 °C cold room overnight. The shape of the gel was cast in customized, 3D printed molds. This technique allowed for the visualization of both the material's viscoplastic flow and the external fluid flow under an illuminated sheet laser. Time-lapse videos at 5 -10 seconds per frame were taken to visualize the plastic deformation of the material under constant fluid shear.

Relevant surfaces and hard plastic streamers were designed and prototyped using 3D printers (Makerbot Replicator 2) and by scanning 3D models made from modeling clay (NextEngine 3D Laser Scanner). Soft streamers were modelled using red colored, 100% cotton strings at different thicknesses and lengths.

Monocultures of cyanobacterium *Leptolyngbya* sp. were cultured using standard medium BG-11 buffered with TES at PH = 8.0.

CHAPTER IV

THE EVOLUTION OF COHESIVE STRENGTH IN MICROBIAL MATS CONTROLLED BY THE EVOLUTION OF OXYGENIC PHOTOSYNTHESIS

IV.1 OVERVIEW

The presence of microbial communities has long been suggested to cause an increase in the cohesive strength of sediment, which is responsible for forming a wide range of microbial-sedimentary structures. Step-wise increase of mat strength towards the end of Archean eon was discovered previously from fossil mats and stromatolites, but it was uncertain what had caused the change. We here suggest that the mechanical strength of mats increased as a direct result of the metabolic switch from an anoxygenic to an oxygenic benthic microbial ecosystem. Support for this hypothesis was provided by examining the strength of experimental mats with productivity limited by various nutrients. In addition, we also expand the record of estimated mat strength beyond the Archean eon. These results add to a growing body of evidence how one single metabolic innovation – oxygenic photosynthesis – forever altered the face of our planet.

IV.2 INTRODUCTION

Microbial colonization can strongly stabilize sediments in modern marine and fluvial environments (Black et al. 2002; Gerbersdorf et al. 2008; Tolhurst et al. 2003). This process produces biosignatures such as oversteepened surfaces in trapping and binding stromatolite lamina, roll-up and rip-up structures eroded from microbial mats,

and mat covered surfaces that resist fluid or gas escape (Grotzinger & Knoll 1999; Schieber 1998; Simonson & Carney 1999; Bosak et al. 2009a; Taj et al. 2014). These structures, although diverse, result from a single emergent physical property of microbial mats: cohesion (Tice et al. 2011). Mat cohesion commonly arises from three major sources: (1) physical entanglement of cell filaments (Gerdes 2007; Gerbersdorf & Wieprecht 2014); (2) secretion of a complex suite of sticky biopolymers (collectively termed extracellular polymeric substances or EPS) (de Winder et al. 1999; de Brouwer et al. 2005; Stal 1995); and (3) promotion of carbonate mineral precipitation and cementation due to EPS sorption of Ca^{2+} (Dupraz et al. 2009).

Mat cohesion estimated from Archean fossil mats and stromatolites (Tice et al. 2011) shows an apparent 4–10-fold increase from the Paleoarchean (3.5 Ga) to the end of the Neoarchean (2.6–2.4 Ga). However, it is not certain what biological or environmental factors might have caused this increase. Strengthening could be the result of (1) an increase of the net productivity of mats with a consequent increase in the content of both cell biomass and EPS in sediments; (2) an enhanced rate of mat cementation during early diagenesis; (3) a change in EPS composition or strength, either through biological evolution or a change in ocean composition; or some combination of any of these.

An intimate connection may exist between the strengthening of mats and a possible increase in net primary productivity at the end of Neoarchean. The transition from predominantly anoxygenic to oxygenic mat communities prior or simultaneous to the 2.3 Ga Great Oxygenation Event (GOE) marks a switch from consuming reductants

such as H_2, CO, HS^- and Fe^{2+} to splitting H_2O as a source of electrons (Lyons et al. 2014). This metabolic innovation likely relieved communities from productivity limitations constrained by the supply of rare electron donors to a much more abundant and accessible electron and hydrogen source, water (Des Marais 2000). Important to add, limitations in electron donors placed more stringent controls on productivity relative to growth limitations determined by levels of nitrogen, phosphorus or iron. This is because electron donors are one-to-three orders of magnitude more effective at directly limiting the amount of carbon that can be fixed. For example, in normal photosynthesis, the CO_2 : e^- donor reaction molar ratio is generally from 1 : 4 to 1 : 2. This means that in order to synthesize one mole of carbon, 2-4 moles of electron donors are required. In contrast, in the nitrogen or phosphorus limited modern ocean, it is the emergent ecological stoichiometry that controls the productivity. This stoichiometry is otherwise termed *Redfield Ratio* for benthic communities: C:N:P = 1 : 0.14 : 0.008 (Hillebrand & Sommer 1999). This means that in order to synthesize one mole of carbon, only 0.14 mole of nitrogen or 0.008 mole of phosphorus is needed – a must less stringent limitation in terms of reaction ratio. Although the Redfield ratio is not necessarily a constant through geologic time, it is rooted deep in the fundamental molecular organization of life such as the protein-to-rRNA ratio (Loladze & Elser 2011). Thus, this ratio is not expected to play a greater role at altering the global net primary productivity in the distant past than it is in the present day. Nonetheless, it is reasonable to suggest that switching to oxygenic photosynthesis had a profound effect on primary productivity. For instance, atmospheric CO_2 could have been drawn down so much (combined with the effect of

rising molecular oxygen that helped to oxidize atmospheric methane through other pathways) that it caused global glaciations several times in the Archean as well as in Paleoproterozoic following GOE (Kopp et al. 2005).

Kharecha et al. (P. Kharecha 2005) estimated that the global net primary productivity likely increased by 20–100 times after the evolution of oxygenic photosynthesis. We further hypothesize that this increase in productivity would have resulted in a significant increase in mat cohesion. Although microorganisms can respond to environmental stimuli by shunting varying amounts of metabolite to EPS production (Stal 1995), the maximum production rate is still limited by net primary production. Biologically promoted carbonate cementation is limited by photosynthetic depletion of interstitial carbonic acid, total EPS abundance, net anaerobic respiration rates below the zone of net productivity, available cell surface area, or some combination of these factors (Dupraz et al. 2009), all of which are limited by net primary productivity. Thus, the maximum potential effectiveness of every major mechanism producing mat strength is set directly or indirectly by the net primary productivity of the mat community. To test how productivity may control sediment strength, we estimated the cohesions of microbial mats grown under a range of nutrient-limiting conditions in the laboratory. Additionally, we extended the record of estimated mat strengths beyond the GOE to include the known span of geologic history over which microbial mats grew.

IV.3 METHODS

IV.3.1 Growth Experiments

Monocultures of the filamentous, mat-forming cyanobacterium *Leptolyngbya* sp. (originally isolated from Yellowstone National Park, Montana, U.S.A: *Leptolyngbya* sp. Y-WT-2000 Cl 1, Culture Collection of Microorganisms from Extreme Environments culture number 5627) were grown on acid-washed quartz sand surfaces under liquid media (VWR Int. Inc.). Cultures were contained in modified 10 mL (~1 cm diameter, 6 cm tall) syringe tubes with the top in free exchange with the atmosphere through a 0.2 µm filter (to maintain a monoculture free from contamination). All cultures were grown under the same temperature and light conditions (42 °C, 12-12-hours regular light-dark cycles). To control mat productivity, a subset of cultures were incubated with reduced nitrogen and phosphorus at $1/50^{th}$ times the concentration of standard medium (BG-11). The same amount of sand was used (~5 mm thick) in each tube and bacteria were inoculated after the deposition of sand. Tubes of different diameters were also used as controls. Detailed drawing and dimensions of these growth tubes are described in Appendix A7.

IV.3.2 Color Index for Chlorophyll-a Measurements

During the experiment, total sediment-bound chlorophyll-a was used as a proxy for sediment biomass (Figure IV.1). RGB color images were obtained with a Pentax K5 DSLR camera under identical light conditions. These were first white-balanced against a known region in the picture with a green tape or an 18% grey card. This further

normalized all the pictures to have the same intensity. Then, a specific color index was developed and tested following a method described by Wang et al. (Wang et al. 2014). Chlorophyll-a was extracted and quantified from a subset of N samples using standard methods (Ritchie 2006) and references therein, with calibrations adapted for cyanobacteria (see detailed protocol in Appendix A9). The significant high correlation (Pearson correlation $r = 0.96$ and p-value $= 8 \times 10^{-7}$) ensured that the color index could be used in place of laboratory chlorophyll extractions (Figure IV.2). Thickness of the mat was estimated by the vertical distribution of chlorophyll-a content (using the same RGB image analysis technique) from the top of the inorganic sediment surface. This information is used to help estimate the failure depth in mats for the calculation of cohesion.

IV.3.3 Carbohydrate Extraction

Total amounts of sediment-bound carbohydrates were extracted and measured from each tube (see Appendix A10). For each tube, liquids were first removed gently with a long needled syringe. Then 5 mL, 5 mM EDTA was added, periodically shaken and incubated in a 42 °C water bath for 20 minutes. This is to extract the sediment-bound EPS. Finally each tubes was centrifuged at 4000 rpm for 10 min, with the supernatant containing dissolved sediment-bound EPS. Method for carbohydrate quantification was based on the standard phenol-sulfuric acid extraction method (Decho et al. 2005; Liu et al. 1973; Underwood et al. 1995; Masuko et al. 2005).

IV.3.4 Cohesive Strength Measurements

In order to establish a metric for sediment cohesion, a sediment-column tilting test was developed by constructing a robotic rotating apparatus designed for pairs of samples (see Appendix A8 for detailed drawings and design). During the test, cohesion was proxied by estimating from video recordings the maximum stable angle of the sediment surface (colonized by microbial mats) relative to an abiotic control tube that was filled with the same liquid medium and sand. Here the abiotic control records the internal angles of friction of the non-cohesive sand. Finally, with failure depths also estimated from the videos, minimum cohesion can be calculated following a formula previously described (Tice et al. 2011):

$$c = \left(\rho_m - \rho\right) g \mathrm{d} \left(\sin\theta - \cos\theta \tan\varphi\right),$$

where ρ_m is the mat density, ρ the water density, g the gravitational acceleration, d the failure depth, θ the maximum stable angle, and φ the internal angle of friction.

IV.3.5. Estimation of Mat Strength in Geologic Records

In order to construct a record of maximum mat strength over time, we estimated mat cohesion or tensile strength for 3–5 layers per sample or published image using the techniques of Tice et al. (Tice et al. 2011). We note here where these techniques were modified. Because maximum cohesion can only be determined in layers closest to failure, the maximum estimate was chosen for each sample. Where multiple samples were available for a single geologic formation, the maximum estimate for the entire formation was chosen. For comparison between estimates of cohesion and tensile

strength, tensile strength was scaled by multiplying tan (30 º) for plotting. This conversion is exact for solids with linear Mohr-Coulomb failure curves and internal angles of friction of 30º.

Slope Cohesion. We estimated original cohesion according to Tice et al. (2011) in laminations that thickened on level paleotopographic highs and thinned on inclined surfaces, or have been otherwise interpreted to have formed through trapping and binding of sediment. Errors in estimated inclination of ±15º yield relative errors in cohesion of ±15–25%, so this technique is not so sensitive to inclination that it cannot be applied to published images without independent field examination. In order to minimize error due to postdepositional deformation, we applied this technique only to stromatolites that were symmetric in cross section.

Trapped Sand Grains. Mats that trap bedload sand grains allow estimation of boundary shear stress, τ, using the Rouse criterion for grains not carried in suspension (Julien 1998), i.e. $\tau < 6.25\omega^2$. Here ω is the terminal fall velocity of the smallest trapped grains, chosen in this study as the tenth percentile grain by diameter in a random sample of ~100 grains.

IV.3.6 Figures

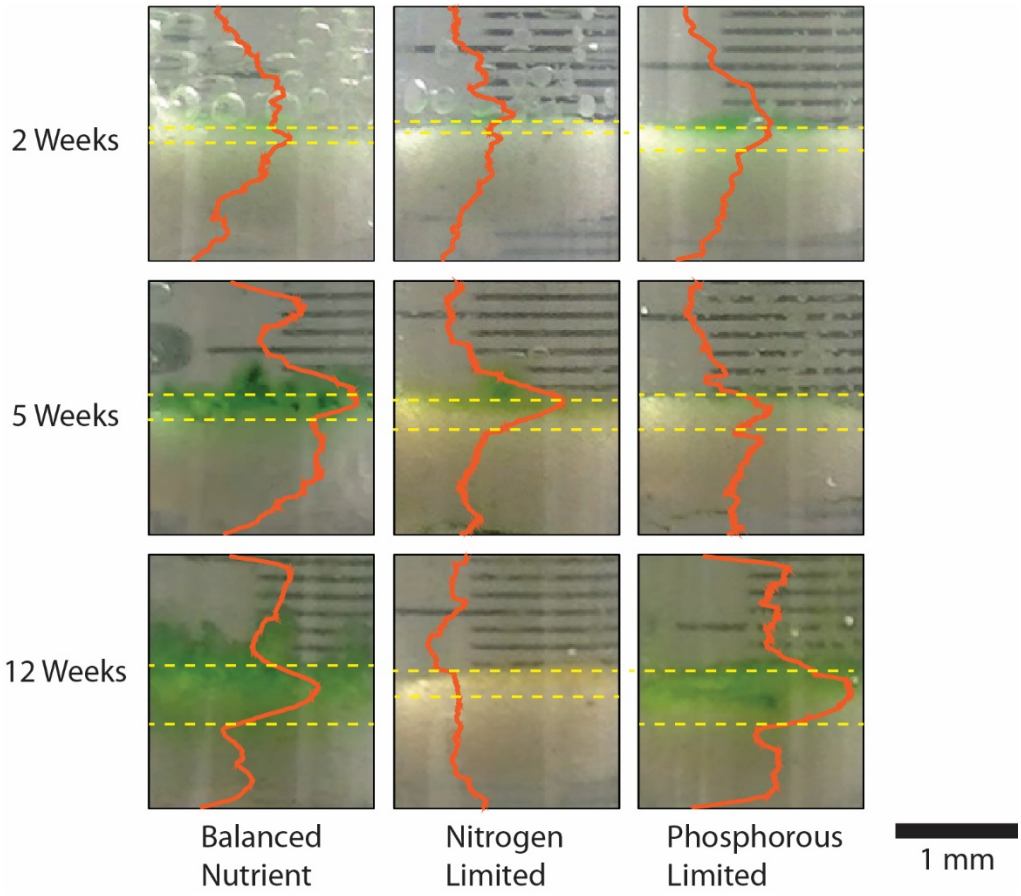

Figure 4.1. Growth matrix in tubes through time (2, 5 and 12 weeks). Nitrogen and Phosphorous limitation were induced by formulating a medium that is 1/50th of the full BG-11 growth medium in the respective nutrient species. Estimated vertical relative distribution of chlorophyll-a content was overlaid on top of each image. This information is used to help estimate the thickness of the sediment colonized by the microbial mat (thickness is measured as the distance between the two dashed lines).

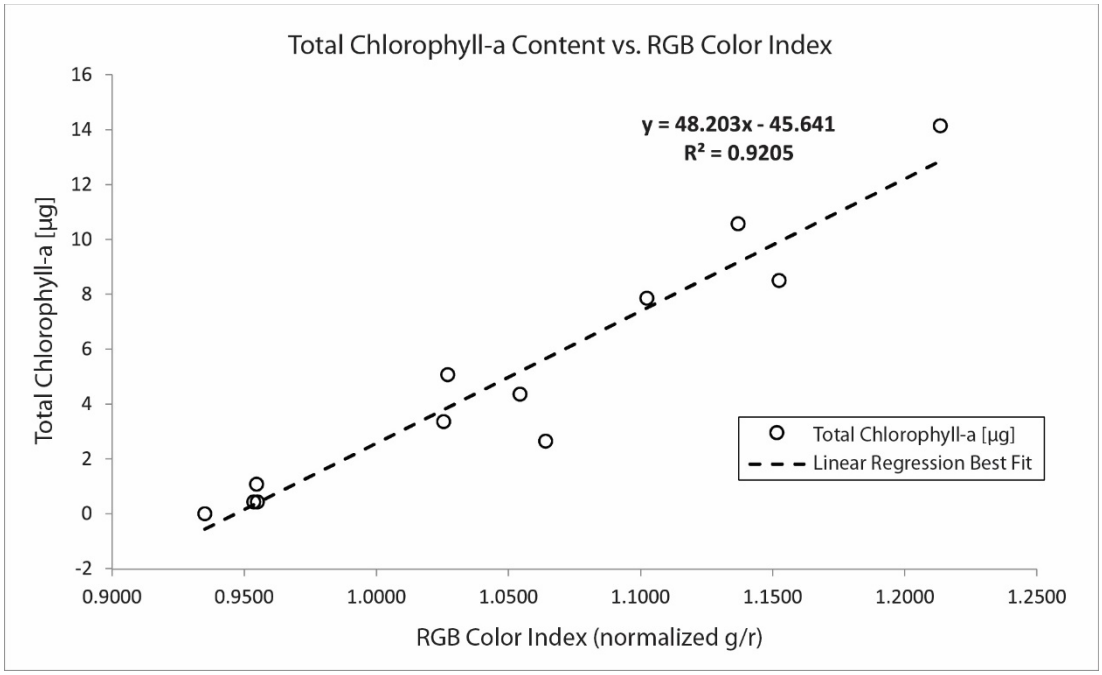

Figure 4.2. Linear regression plot between total chlorophyll-a content and a color index based on RGB color-space (see Methods 2 for details on the color index development). 12 samples (three replicas each) were used to cover the range of the total chlorophyll-a content measured in all experiments. Linear regression analysis gives a Pearson correlation r = 0.96, R^2 = 0.92 and p-value = 8×10^{-7}.

IV.4 RESULTS

As time progresses, different nutrient profiles resulted in different productivity as expected (productivity was proxied with chlorophyll-a content in Figure 4.3A). Under nitrogen or phosphorus limitations, cellular biomass experienced declines between 2-5 weeks. Subsequently, phosphorus-limited mats continued to grow until 12 weeks while nitrogen-limited mats declined in biomass after 5 weeks. On the other hand, total sediment-bound carbohydrate did not show significant declines under nutrient limitation (Figure 4.3B). This is also reflected in the ratio of carbohydrate and chlorophyll-a (Figure 4.3C). Without nutrient limitations, sediments generally accumulated more carbohydrate per unit biomass in time. This corresponded to an increase in sediment strength over time, as shown in Figure 4.3D. Thus, this set of results demonstrated that carbohydrate content is more directly responsible for sediment cohesive strength, rather than living cell biomass.

Sediment-bound carbohydrate content also correlated strongly with sediment cohesion across all samples, with a highly significant p-value of 1.1×10^{-6} (Figure 4.4A). Correlating between chlorophyll-a (living sediment-bound biomass) and sediment strength gave a p-value of 1.1×10^{-3}, although the adjusted R-square value was only 0.31, suggesting that the chlorophyll-a data alone may not be sufficient to explain all the variations observed. Correlating total carbohydrate (proxy for EPS) with total chlorophyll-a (proxy for biomass) (Figure 4.4B) showed that under nutrient starvation in nitrogen and phosphorous, no significant trend exists between carbohydrate and chlorophyll-a. However under balanced nutrients, the correlation is strong (*p*-value =

0.005). These results showed that nutrient limitation had a significant effect on productivity, which in turn controlled both biomass and carbohydrate production.

In the geologic record, mat strength increased abruptly at 2.73 Ga and remained high for most of Earth history when stromatolites formed abundantly. Maximum mat strength increased between 2.73–2.52 Ga from Paleoarchean and Mesoarchean lows of 0.5–9 Pa to Neoarchean and Proterozoic highs of ~30–50 Pa (Figure 4.5). Elevated mat strengths (13–50 Pa) were first developed in cuspate and tent-like mats unique to the interval 2.73–2.52 Ga but widespread in low-energy subtidal environments of that time (Murphy & Sumner 2008). In contrast, stromatolite-forming mats in higher-energy environments did not begin to develop elevated strength (14–20 Pa) until 2.64–2.52 Ga, and did not approach maximum strengths exhibited by cuspate mats until 2.0–1.9 Ga. Maximum mat strengths remained high for the rest of geologic time during intervals when stromatolites were abundant, but are relatively low in modern settings (0.3–13 Pa).

To compare strengths of mats from different times, we divided the data into four groups: 1) mats formed at or before 2.65 Ga (N = 10), 2) cuspate and tent-like mats formed 2.73–2.52 Ga (N = 4), 3) mats formed 2.52–0.10 Ga (N = 26), and 4) modern mats (N = 8). These groups exhibit significant variation (Kruskal-Wallis test, $p=5\times10^{-5}$). To detect variation between specific groups, we performed *post hoc* two-tailed Mann-Whitney tests (Appendix A11). Cuspate and tent-like mats formed 2.73–2.52 Ga and mats formed 2.52–0.10 Ga were significantly stronger than mats formed at or before 2.65 Ga and modern mats. No other significant pair-wise differences were detected.

IV.4.1 Figures

Figure 4.3. Time series of mat development. (A) Chlorophyll-a. (B) Sediment-bound carbohydrate. (C) Ratio of carbohydrate and chlorophyll-a. (D) Cohesive strength of the sediment estimated as the maximum relative stability angle. All horizontal axes represent the incubation time (in weeks).

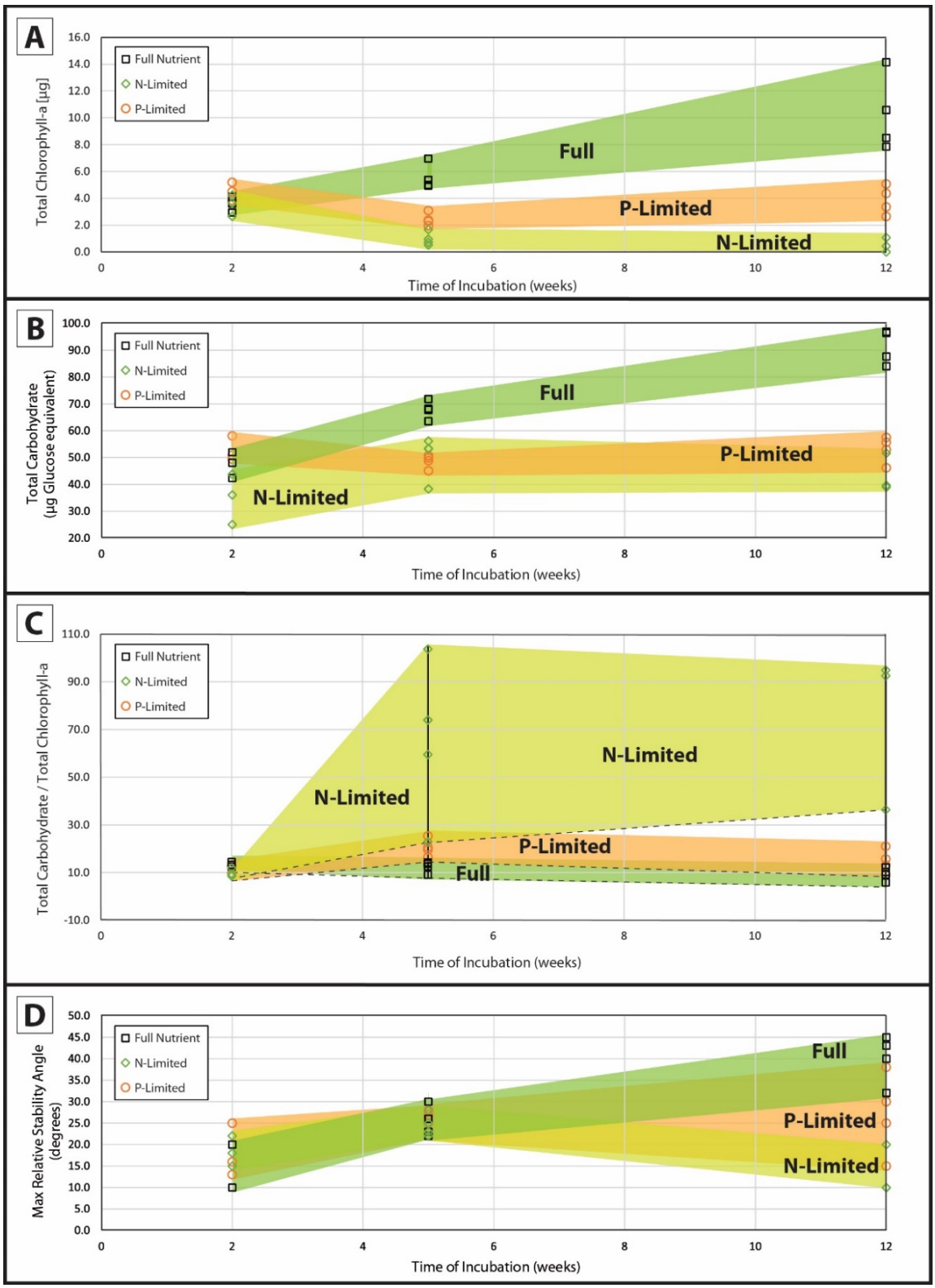
A
Total Chlorophyll-a [µg]
Full Nutrient
N-Limited
P-Limited
Full
P-Limited
N-Limited
Time of Incubation (weeks)
B
Total Carbohydrate (µg Glucose equivalent)
Full Nutrient
N-Limited
P-Limited
Full
P-Limited
N-Limited
Time of Incubation (weeks)
C
Total Carbohydrate / Total Chlorophyll-a
Full Nutrient
N-Limited
P-Limited
N-Limited
N-Limited
P-Limited
Full
Time of Incubation (weeks)
D
Max Relative Stability Angle (degrees)
Full Nutrient
N-Limited
P-Limited
Full
P-Limited
N-Limited
Time of Incubation (weeks)

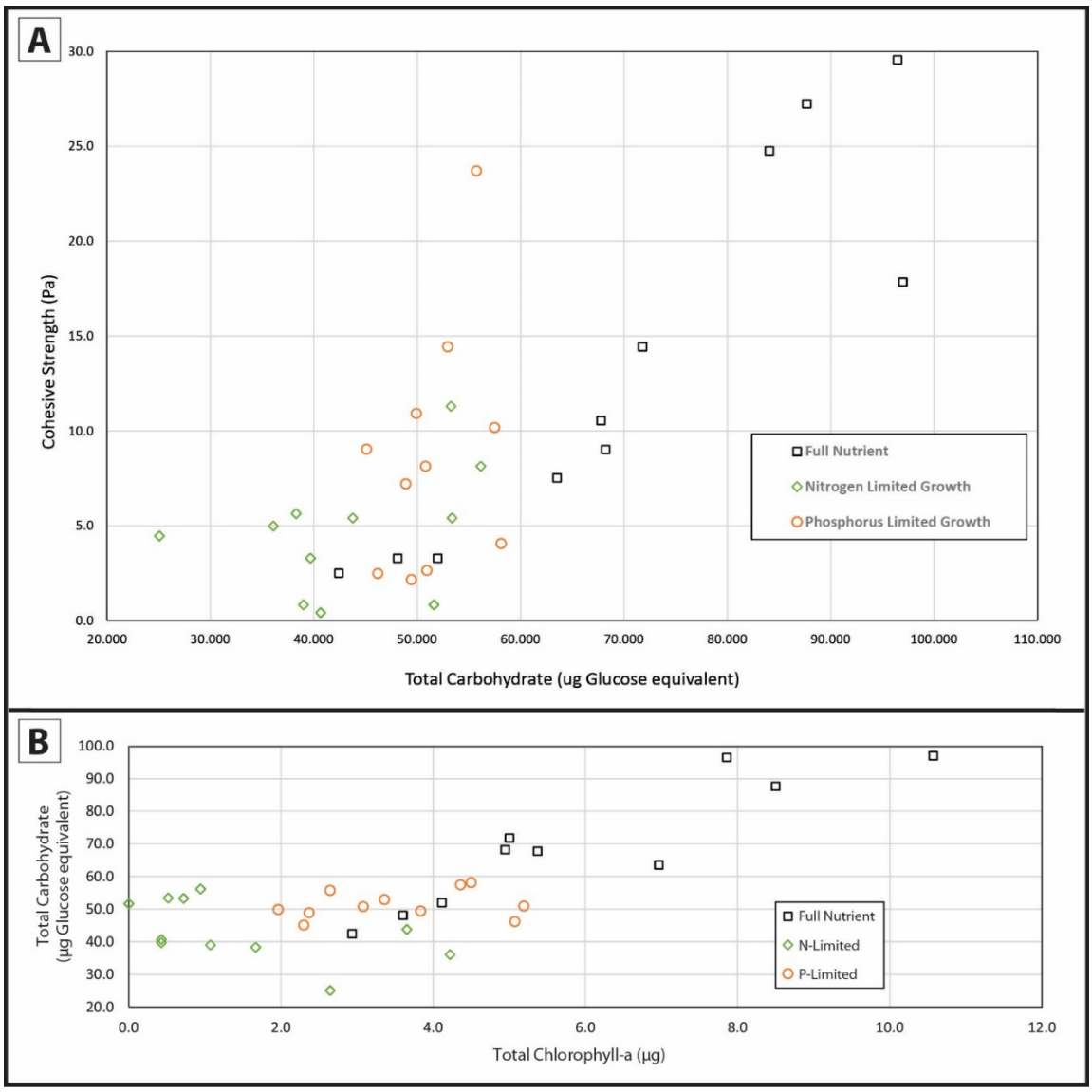

Figure 4.4. Carbohydrate content in connection with sediment cohesion as well as cell biomass. (A) Scatter plot between carbohydrate content and cohesive strength, estimated in Pascals from tilting experiments. (B) Scatter plot between total sediment-bound carbohydrate and total chlorophyll-a.

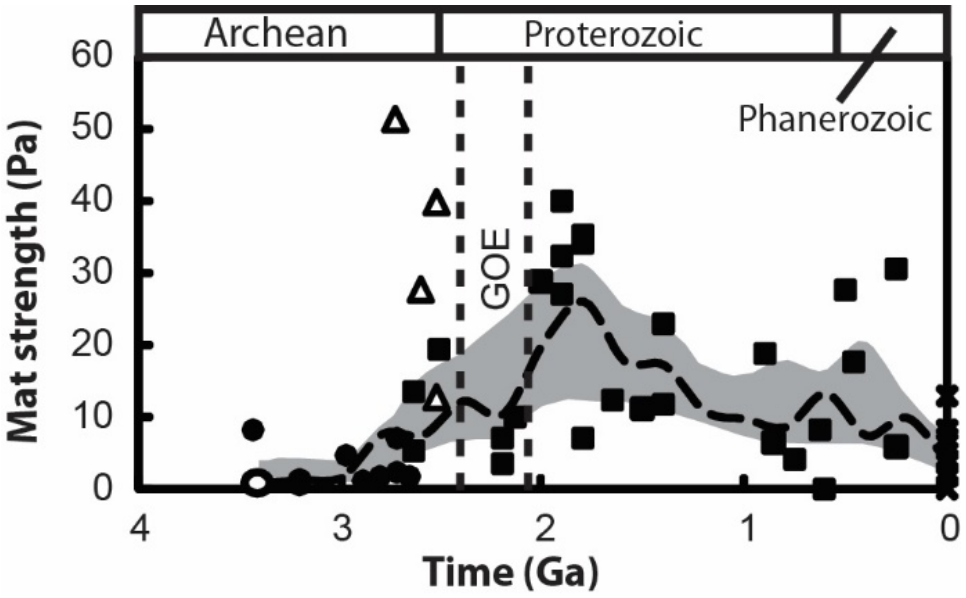

Figure 4.5. Maximum mat strengths through Earth history. Cohesion is plotted as filled symbols; tensile strengths are scaled by tan (30º) and plotted as open symbols. Circles = mats at or before 2.65 Ga; triangles = cuspate and tent-like mats; squares = mats from 2.65–0.10 Ga; crosses = modern mats. Dashed line shows median loess local regression (tri-cube weight function, smoothing parameter of 0.33). Shaded area denotes 68% confidence intervals on the regression (bootstrap analysis). Mat strength increased abruptly at 2.73 Ga and remained high for most of Earth history when stromatolites formed abundantly. Modern mat communities are relatively weak. Data table and references are included in Appendix A13.

IV.5 DISCUSSION

Although anoxygenic photosynthesis is certainly less productive than oxygenic photosynthesis, this is irrelevant to the hypothesis that mat strength is controlled largely by productivity. Given time, sufficient nutrients, and unlimited supply of electron donors, any mat could potentially grow to become highly cohesive, regardless of the metabolic pathways of the microbes creating it. Therefore, mat strength represents a common state of a microbial ecosystem rather than specific scenarios. Such properties are best tested with a well-understood model system (Tanja Bosak 2012).

Production of carbohydrates is a fundamental process by which microorganisms construct extracellular matrix in support of a community life style. In this process, polysaccharide secreted outside of cells becomes a structural molecule that provides microbial mats structural strength and elasticity. Our monoculture experiments also suggest that EPS could still be present after living biomass is no longer available, sustaining sediment strength. However, we acknowledge that our experiments included only a single strain of bacteria in contrast to the diverse populations of microbes occurring in natural sediments. Ours is a model system designed to test a specific hypothesis. In reality, carbohydrates are a carbon and energy source for the entire mat ecosystem and the breakdown of EPS may also negatively affect sediment stabilization, reducing mat cohesion in some cases while enhancing strength in others through induced cementation.

The increase in mat strength at 2.73 Ga likely resulted from a change in the physical entanglement of community members, the production of EPS, the rate of mat

cementation, or some combination of these factors. A change in physical entanglement is unlikely since fossils of filamentous microorganisms, the most common components of entangled fabrics, are known from rocks as old as 3.47 Ga (Walsh 1992). A change in cementation due solely to evolving seawater composition is also unlikely given the step-like transition observed at 2.73 Ga. Moreover, the first high-strength communities formed draping organic films over open voids and probably inhibited carbonate mineral precipitation during growth (Sumner 1997). Although voids were ultimately filled with calcite, implying that cementation played a critical role in preserving these structures, precipitation during growth did not provide significant tensile strength or cohesion. These structures are more than ten times as large and strong as draping fossil mats preserved by early silica precipitation from 3.42 Ga (Tice et al. 2011), suggesting that the sudden appearance of high-strength communities was not a product of differential preservation. Instead, increased mat strength appears to have resulted from enhancement of biological or biologically-promoted processes, most likely as an indirect consequence of the emergence of cyanobacterial communities.

Significantly, conical stromatolites preserve fenestrae in their apices representing gas-filled voids beginning at 2.73 Ga (Bosak et al. 2009b), coincident with the first high-strength communities (Figure 4.5). Bosak et al. (2009b) argue that the primary gas in these voids was oxygen based on the positions of the fenestrae in the highest positions in these stromatolites. We suggest that the appearance of these morphological features and the simultaneous step-wise increase in mat strength mark the emergence of benthic cyanobacterial communities. Geochemical evidence suggests a possible small initial

release of oxygen to the atmosphere at ~2.7 Ga (Frei et al. 2009) and increased incorporation of methanogenic carbon into sedimentary organic matter at the same time (Hayes 1984), a predicted result of initial oxygen generation. A Neoarchean origin of cyanobacterial communities is consistent with the presence of open marine anoxygenic photosynthetic communities at 3.42 Ga (Tice & Lowe 2006).

The paleoenvironmental distribution of the earliest high-strength communities and fenestrae-forming conical stromatolites suggests that the first cyanobacteria competed with anoxygenic phototrophs for resources in the euphotic zone. In particular, both communities grew in low-energy subtidal environments where substrate transport was probably limited by slow diffusion (Alexander P. Petroff et al. 2010a; Sumner 1997). Under these conditions, primitive oxygenic organisms making inefficient or occasional use of water would have been at greatest advantage relative to photosynthetic organisms using rare reductants such as H_2, HS^-, or Fe^{2+}. A deep-water habitat for early cyanobacteria is consistent with the low-light sensitivity of *Gloeobacter violaceus* (Koenig & Schmidt 1995), strongly supported to be the lowest-branching organism in the cyanobacterial tree (Swingley et al. 2008). In this organism, low-light adaptation is hypothesized to be a property of primitive characters of the photosynthetic apparatus (Koyama et al. 2008).

As the first cyanobacteria became more proficient at harvesting electrons from water, they would have come to dominate higher-energy environments as well, a transition likely recorded by increasing stromatolite strength beginning ~2.64–2.52 Ga and by the appearance of large barrier reefs at 2.52 Ga (Grotzinger 2000). Increasing

efficiency and productivity of shallow-water cyanobacterial communities may also be recorded by the oxygenation of shallow-water environments beginning at ~2.50 Ga (Anbar et al. 2007; Kaufman et al. 2007; Scott et al. 2008), and ultimately by accelerating oxygenation of the atmosphere beginning at 2.45–2.32 Ga (Bekker et al. 2004). In this model, competition with incumbent anoxygenic phototrophs initially limited the distribution of the first cyanobacteria as well as their effectiveness in oxygenating surface environments.

Our experimental monoculture mats reached a cohesion of around 30 Pa, stronger than most modern mats estimated. Modern mats also are confined to extreme environments that exclude multicellular algae and grazing metazoans. Seaweed stipes have tensile strengths on the order of 10^7 Pa (Pratt & Johnson 2002), much greater than the highest strengths estimated for microbial sediments. Greater strength allows them to outcompete mats for light and nutrients in essentially any flow by constructing differentiated photosynthetic structures which project above the sediment surface. Restriction to relatively low-energy stressful environments likely limits the strengths of modern mat communities, making them good models for many of the low-strength mats in the geologic record and essentially all mats inferred to be anoxygenic prior to 2.73 Ga. However, many Neoarchean and Proterozoic stromatolite-forming cyanobacterial mats may have no quantitative modern natural analogues.

This analysis suggests that the oxygenation of early surface environments may have been associated with an increasing cyanobacterial oxygen source rather than with decreasing oxygen sinks, but that increases were extended over the course of about 300–

400 Myr ahead of rather than during the geologically short Great Oxidation Event. Instead of rapidly dominating the euphotic zone, cyanobacteria first formed communities in quiet-water environments. The ultimate oxygenation of the atmosphere at 2.45–2.32 Ga was triggered by the cyanobacterial conquest of broad high-energy shelf and reef environments.

IV.6 CONCLUSION

Cohesive strength is an emergent material property of a microbial ecosystem that results from accumulation of EPS in the sediment. In this case, carbohydrate was likely an important class of structuring molecule in the matrix to providing strength. Significantly, cohesive strength was found to correlate positively with the productivity of a common cyanobacterium *Leptolyngbya* sp. that form mats. By extending the record of mats strength over geologic time, a compressive picture of mat ecosystem productivity through time was re-constructed. In this data set, we associate the most abrupt jump of cohesion increase around 2.73 Ga with the most profound metabolic switch in the history of life on Earth, the expansion of oxygenic photosynthesis.

CHAPTER V

SUMMARY

Microorganisms do extraordinary things when they form communities. Understanding these emergent phenomena in specific contexts helps us to understand the marks they left in the fossil record. The accumulation of these specific knowledge also enables us to infer the larger environment to which they adapted and evolved in the long and complex geologic record.

In this dissertation, I explored the physical principles by which several unique shapes are constructed in sedimentary environments where microbial communities dominate. Specifically, the feedbacks between those physical and biological processes are understood under a guiding theoretical framework of the principle of environmental fluid flow as well as the theory of material science. The deep connections between these disciplines continue to guide further research in the years to come.

In understanding how conical mats form from a filamentous cyanobacterial community in a diffusion-transport dominated environment, we uncovered some extraordinary social behaviors of the communities, including that these bacteria may sense each other's presence by touch, and are able to trigger social behaviors based on population density and regulate group activities in synchrony. Specifically, when groups of organisms aggregate and disaggregate, sand grains underneath the mats are rolled and sorted into specific patterns. These patterns were discovered in fossil records of Archean tidal microbial communities, demonstrating the antiquity of such multicellular behaviors.

In attempting to resolve how microbial streamers may form in erosive, high shear flows, we discovered some unique feedbacks between turbulent fluid forcing and the deformation of microbial mats around complex geometries. In this case, with enough flow strength and surface roughness, deformation of mats at the top of surface protrusions ultimately initialize streamers. Additionally, streamers are not always the roughness elements that we intuitively thought they were, on the contrary, they commonly self-organize to reattach broken boundary layers and hydraulically smooth the flow. This is a common process how streamers form and interact with erosive flows.

Finally, in evaluating how sediments became cohesive when inhabited by microbial communities, we discovered that the cohesion of mats is largely controlled by the amount of carbohydrates in the sediment. This cohesion is directly linked to the productivity of the community. In addition, by extending the record of estimated mat strength over most of the geologic history, we re-construct a comprehensive picture of the history of mat ecosystem productivity. Significantly, a step-wise mat strength increase around 2.73 Ga was associated with the expansion of oxygenic photosynthesis in benthic ecosystems.

REFERENCES

Aguet, F., Van De Ville, D. & Unser, M., 2008. Model-Based 2.5-D Deconvolution for Extended Depth of Field in Brightfield Microscopy. *IEEE Transactions on Image Processing*, 17(7), pp.1144–1153.

Allwood, A.C. et al., 2006. Stromatolite Reef from the Early Archaean Era of Australia. *Nature*, 441(7094), pp.714–718.

Allwood, A.C., Hodyss, R. & Wade, L., 2012. Micro-XRF: Elemental Analysis for in Situ Geology and Astrobiology Exploration. *LPI Contributions*, 1683, p.1138.

Anbar, A.D. et al., 2007. A Whiff of Oxygen Before the Great Oxidation Event? *Science*, 317(5846), pp.1903–1906.

Balagam, R. et al., 2014. Myxococcus Xanthus Gliding Motors Are Elastically Coupled to the Substrate as Predicted by the Focal Adhesion Model of Gliding Motility. *PLoS Computational Biology*, 10(5). Available at: http://www.ncbi.nlm.nih.gov/pmc/articles/PMC4014417/ [Accessed March 6, 2015].

Bangerth, W. et al., 2015. The dealii Library, Version 8.2. *Archive of Numerical Software*, 3(1). Available at: http://journals.ub.uni-heidelberg.de/index.php/ans/article/view/18031 [Accessed May 31, 2015].

Bangerth, W., Hartmann, R. & Kanschat, G., 2007. Deal.ii—a General-Purpose Object-Oriented Finite Element Library. *ACM Trans. Math. Softw.*, 33(4). Available at: http://doi.acm.org/10.1145/1268776.1268779 [Accessed May 31, 2015].

Bekker, A. et al., 2004. Dating the Rise of Atmospheric Oxygen. *Nature*, 427(6970), pp.117–120.

Berg, H.C., 1993. *Random Walks in Biology* Revised edition., Princeton, N.J: Princeton University Press.

Black, K. et al., 2002. Working with Natural Cohesive Sediments. *Journal of Hydraulic Engineering*, 128(1), pp.2–8.

Bosak, T. et al., 2012. Cyanobacterial Diversity and Activity in Modern Conical Microbialites. *Geobiology*, 10(5), pp.384–401.

Bosak, T. et al., 2009a. Morphological Record of Oxygenic Photosynthesis in Conical Stromatolites. *Proceedings of the National Academy of Sciences*, 106(27), pp.10939–10943.

Bosak, T. et al., 2009b. Morphological Record of Oxygenic Photosynthesis in Conical Stromatolites. *Proceedings of the National Academy of Sciences*, 106(27), pp.10939–10943.

Branda, S.S. et al., 2001. Fruiting Body Formation by Bacillus Subtilis. *Proceedings of the National Academy of Sciences*, 98(20), pp.11621–11626.

Brevis, W., Niño, Y. & Jirka, G.H., 2010. Integrating Cross-Correlation and Relaxation Algorithms for Particle Tracking Velocimetry. *Experiments in Fluids*, 50(1), pp.135–147.

de Brouwer, J.F.C. de et al., 2005. Biogenic Stabilization of Intertidal Sediments: The Importance of Extracellular Polymeric Substances Produced by Benthic Diatoms. *Microbial Ecology*, 49(4), pp.501–512.

Cabral, B. & Leedom, L.C., 1993. Imaging Vector Fields Using Line Integral Convolution. In *Proceedings of the 20th Annual Conference on Computer Graphics and Interactive Techniques*. SIGGRAPH '93. New York, NY, USA: ACM, pp. 263–270. Available at: http://doi.acm.org/10.1145/166117.166151 [Accessed June 3, 2015].

Castenholz, R.W., 1988. Culturing Methods for Cyanobacteria. In A. N. G. Lester Packer, ed. *Methods in Enzymology*. Cyanobacteria. Academic Press, pp. 68–93. Available at: http://www.sciencedirect.com/science/article/pii/0076687988670066 [Accessed June 7, 2014].

Chayes, F., 1956. *Petrographic Modal Analysis*, John Wiley And Sons Limited. Available at: http://archive.org/details/petrographicmoda033289mbp [Accessed February 20, 2015].

Cheel, R.J., 1984. Heavy Mineral Shadows, a New Sedimentary Structure Formed Under Upper-Flow-Regime Conditions; Its Directional and Hydraulic Significance. *Journal of Sedimentary Research*, 54(4), pp.1175–1182.

Decho, A.W., Visscher, P.T. & Reid, R.P., 2005. Production and Cycling of Natural Microbial Exopolymers (EPS) within a Marine Stromatolite. *Palaeogeography, Palaeoclimatology, Palaeoecology*, 219(1–2), pp.71–86.

Des Marais, D.J., 2000. When Did Photosynthesis Emerge on Earth? *Science*, 289(5485), pp.1703–1705.

Dietrich, L.E.P., Tice, M.M. & Newman, D.K., 2006. The Co-Evolution of Life and Earth. *Current Biology*, 16(11), pp.R395–R400.

Dupraz, C. et al., 2009. Processes of Carbonate Precipitation in Modern Microbial Mats. *Earth-Science Reviews*, 96(3), pp.141–162.

Edwards, K.J. et al., 2000. An Archaeal Iron-Oxidizing Extreme Acidophile Important in Acid Mine Drainage. *Science*, 287(5459), pp.1796–1799.

Flannery, D.T. & Walter, M.R., 2012. Archean Tufted Microbial Mats and the Great Oxidation Event: New Insights into an Ancient Problem. *Australian Journal of Earth Sciences*, 59(1), pp.1–11.

Flot, J.-F. & Cady, S.L., 2002. Formation of thermophilic streamer biosignatures, Yellowstone National Park, USA. Celnikier, L. & J. Tran Thanh Van, eds. *Frontiers of Life, proceedings of the 12th Rencontres de Blois*, pp.135–137.

Forster, B. et al., 2004. Complex Wavelets for Extended Depth-of-Field: A New Method for the Fusion of Multichannel Microscopy Images. *Microscopy Research and Technique*, 65(1-2), pp.33–42.

Frei, R. et al., 2009. Fluctuations in Precambrian Atmospheric Oxygenation Recorded by Chromium Isotopes. *Nature*, 461(7261), pp.250–253.

Gamper, A. et al., 2012. Composition and Microfacies of Archean Microbial Mats (Moodies Group, Ca. 3.22 Ga, South Africa). In N. Noffke & H. Chafetz, eds. *Microbial Mats in Siliciclastic Depositional Systems Through Time*. Tulsa: S E P M - Soc Sedimentary Geology, pp. 65–74.

Gerbersdorf, S.U. et al., 2008. Microbial Stabilization of Riverine Sediments by Extracellular Polymeric Substances. *Geobiology*, 6(1), pp.57–69.

Gerbersdorf, S.U. & Wieprecht, S., 2014. Biostabilization of Cohesive Sediments: Revisiting the Role of Abiotic Conditions, Physiology and Diversity of Microbes, Polymeric Secretion, and Biofilm Architecture. *Geobiology*, p.n/a–n/a.

Gerdes, G., 2007. Structures Left by Modern Microbial Mats in Their Host Sediments. *Atlas of microbial mat features preserved within the siliciclastic rock record*, pp.5–38.

Gerdes, G., Klenke, T. & Noffke, N., 2000. Microbial Signatures in Peritidal Siliciclastic Sediments: A Catalogue. *Sedimentology*, 47(2), pp.279–308.

Geuzaine, C. & Remacle, J.-F., 2009. Gmsh: A 3-D finite element mesh generator with built-in pre- and post-processing facilities. *International Journal for Numerical Methods in Engineering*, 79(11), pp.1309–1331.

Gong, J., Zeng, Z. & Tice, M., 2015. Formation of Conical Mats by Socially Motile Filamentous Bacteria by 3.22 Billion Years Ago. Available at: http://figshare.com/s/929f685ac5d211e4bae406ec4b8d1f61.

Grotzinger, J.P., 2000. Precambrian Carbonates: Evolution of Understanding. Available at: http://archives.datapages.com/data/sepm_sp/SP67/Precambrian_Carbonates_Evolution_of_Understanding.html [Accessed September 25, 2015].

Grotzinger, J.P. & Knoll, A.H., 1999. Stromatolites in Precambrian Carbonates: Evolutionary Mileposts or Environmental Dipsticks? *Annual Review of Earth and Planetary Sciences*, 27, pp.313–358.

Hall-Stoodley, L., Costerton, J.W. & Stoodley, P., 2004. Bacterial Biofilms: From the Natural Environment to Infectious Diseases. *Nature Reviews Microbiology*, 2(2), pp.95–108.

Hayes, J.M., 1984. Global Methanotrophy at the Archean-Preoterozoic Transition. In S. Bengtson, ed. New York, NY, USA: Columbia University Press.

Heubeck, C., 2009. An Early Ecosystem of Archean Tidal Microbial Mats (moodies Group, South Africa, Ca. 3.2 Ga). *Geology*, 37(10), pp.931–934.

Hillebrand, H. & Sommer, U., 1999. The Nutrient Stoichiometry of Benthic Microalgal Growth: Redfield Proportions Are Optimal. *Limnology and Oceanography*, 44(2), pp.440–446.

Hofmann, H.J. et al., 1999. Origin of 3.45 Ga Coniform Stromatolites in Warrawoona Group, Western Australia. *Geological Society of America Bulletin*, 111(8), pp.1256–1262.

Jørgensen, B.B., 1994. Diffusion Processes and Boundary Layers in Microbial Mats. In L. J. Stal & P. Caumette, eds. *Microbial Mats*. NATO ASI Series. Springer Berlin Heidelberg, pp. 243–253. Available at: http://link.springer.com/chapter/10.1007/978-3-642-78991-5_25 [Accessed May 30, 2015].

Julien, P.Y., 1998. Erosion and Sedimentation. *Cambridge University Press*. Available at: http://www.cambridge.org/us/academic/subjects/earth-and-environmental-science/sedimentology-and-stratigraphy/erosion-and-sedimentation-2nd-edition?format=PB [Accessed September 25, 2015].

Kaufman, A.J. et al., 2007. Late Archean Biospheric Oxygenation and Atmospheric Evolution. *Science*, 317(5846), pp.1900–1903.

Kay, C.M. et al., 2013. Evolution of Microbial “Streamer” Growths in an Acidic, Metal-Contaminated Stream Draining an Abandoned Underground Copper Mine. *Life*, 3(1), pp.189–210.

Knoll, A.H., Canfield, D.E. & Konhauser, K.O., 2012. *Fundamentals of Geobiology*, John Wiley & Sons.

Koenig, F. & Schmidt, M., 1995. Gloeobacter Violaceus— Investigation of an Unusual Photosynthetic Apparatus. Absence of the Long Wavelength Emission of Photosystem I in 77 K Fluorescence Spectra. *Physiologia Plantarum*, 94(4), pp.621–628.

Kopp, R.E. et al., 2005. The Paleoproterozoic Snowball Earth: A Climate Disaster Triggered by the Evolution of Oxygenic Photosynthesis. *Proceedings of the National Academy of Sciences of the United States of America*, 102(32), pp.11131–11136.

Koyama, K. et al., 2008. Oxygen Evolution in the Thylakoid-Lacking Cyanobacterium Gloeobacter Violaceus Pcc 7421. *Biochimica et Biophysica Acta (BBA) - Bioenergetics*, 1777(4), pp.369–378.

Lau, E. et al., 2005. Molecular Diversity of Cyanobacteria Inhabiting Coniform Structures and Surrounding Mat in a Yellowstone Hot Spring. *Astrobiology*, 5(1), pp.83–92.

Lin, L.-H. et al., 2006. Long-Term Sustainability of a High-Energy, Low-Diversity Crustal Biome. *Science*, 314(5798), pp.479–482.

Liu, D., Wong, P.T.S. & Dutka, B.J., 1973. Determination of Carbohydrate in Lake Sediment by a Modified Phenol-Sulfuric Acid Method. *Water Research*, 7(5), pp.741–746.

Loladze, I. & Elser, J.J., 2011. The Origins of the Redfield Nitrogen-to-Phosphorus Ratio Are in a Homoeostatic Protein-to-Rrna Ratio. *Ecology Letters*, 14(3), pp.244–250.

Lowe, D.R., 1980. Stromatolites 3,400-Myr old from the Archean of Western Australia. *Nature*, 284(5755), pp.441–443.

Lundvall, M., 2013. *Yet Another Webcam Software (Yawcam)*, Available at: http://www.yawcam.com/index.php [Accessed March 14, 2014].

Lyons, N.A. & Kolter, R., 2015. On the Evolution of Bacterial Multicellularity. *Current Opinion in Microbiology*, 24, pp.21–28.

Lyons, T.W., Reinhard, C.T. & Planavsky, N.J., 2014. The Rise of Oxygen in Earth's Early Ocean and Atmosphere. *Nature*, 506(7488), pp.307–315.

Marty, A. et al., 2012. Formation of bacterial streamers during filtration in microfluidic systems. *Biofouling*, 28(6), pp.551–562.

Masuko, T. et al., 2005. Carbohydrate Analysis by a Phenol–Sulfuric Acid Method in Microplate Format. *Analytical Biochemistry*, 339(1), pp.69–72.

Murphy, M.A. & Sumner, D.Y., 2008. Variations in Neoarchean Microbialite Morphologies: Clues to Controls on Microbialite Morphologies Through Time. *Sedimentology*, 55(5), pp.1189–1202.

Noffke, N., 2015. Ancient Sedimentary Structures in the <3.7 Ga Gillespie Lake Member, Mars, That Resemble Macroscopic Morphology, Spatial Associations, and Temporal Succession in Terrestrial Microbialites. *Astrobiology*, 15(2), pp.169–192.

Noffke, N. et al., 2006. A New Window into Early Archean Life: Microbial Mats in Earth's Oldest Siliciclastic Tidal Deposits (3.2 Ga Moodies Group, South Africa). *Geology*, 34(4), pp.253–256.

Parsek, M.R. & Singh, P.K., 2003. Bacterial Biofilms: An Emerging Link to Disease Pathogenesis. *Annual Review of Microbiology*, 57, pp.677–701.

Petroff, A.P. et al., 2010. Biophysical Basis for the Geometry of Conical Stromatolites. *Proceedings of the National Academy of Sciences*, 107(22), pp.9956–9961.

Petroff, A.P. et al., 2010a. Biophysical Basis for the Geometry of Conical Stromatolites. *Proceedings of the National Academy of Sciences*, 107(22), pp.9956–9961.

Petroff, A.P. et al., 2010b. Biophysical basis for the geometry of conical stromatolites. *Proceedings of the National Academy of Sciences*, 107(22), pp.9956–9961.

Picologlou, B.F., Characklis, W.G. & Zelver, N., 1980. Biofilm Growth and Hydraulic Performance. *Journal of the Hydraulics Division*, 106(5), pp.733–746.

P. Kharecha, K.J., 2005. A Coupled Atmosphere–Ecosystem Model of the Early Archean Earth. *Geobiology*, 3(2), pp.53 – 76.

Pratt, M.C. & Johnson, A.S., 2002. Strength, Drag, and Dislodgment of Two Competing Intertidal Algae from Two Wave Exposures and Four Seasons. *Journal of Experimental Marine Biology and Ecology*, 272(1), pp.71–101.

Reyes, K. et al., 2013. Surface Orientation Affects the Direction of Cone Growth by Leptolyngbya Sp. Strain C1, a Likely Architect of Coniform Structures Octopus Spring (yellowstone National Park). *Applied and Environmental Microbiology*, 79(4), pp.1302–1308.

Reysenbach, A.-L. & Cady, S.L., 2001. Microbiology of ancient and modern hydrothermal systems. *Trends in Microbiology*, 9(2), pp.79–86.

Ritchie, R.J., 2006. Consistent Sets of Spectrophotometric Chlorophyll Equations for Acetone, Methanol and Ethanol Solvents. *Photosynthesis Research*, 89(1), pp.27–41.

Rusconi, R. et al., 2010. Laminar Flow Around Corners Triggers the Formation of Biofilm Streamers. *Journal of the Royal Society Interface*, 7(50), pp.1293–1299.

Rusconi, R. et al., 2011. Secondary Flow as a Mechanism for the Formation of Biofilm Streamers. *Biophysical Journal*, 100(6), pp.1392–1399.

Schieber, J., 1998. Possible Indicators of Microbial Mat Deposits in Shales and Sandstones: Examples from the Mid-Proterozoic Belt Supergroup, Montana, U.s.a. *Sedimentary Geology*, 120(1–4), pp.105–124.

Schindelin, J. et al., 2012. Fiji: An Open-Source Platform for Biological-Image Analysis. *Nature Methods*, 9(7), pp.676–682.

Schneider, C.A., Rasband, W.S. & Eliceiri, K.W., 2012. NIH Image to Imagej: 25 Years of Image Analysis. *Nature Methods*, 9(7), pp.671–675.

Scott, C. et al., 2008. Tracing the Stepwise Oxygenation of the Proterozoic Ocean. *Nature*, 452(7186), pp.456–459.

Sim, M.S. et al., 2012. Oxygen-Dependent Morphogenesis of Modern Clumped Photosynthetic Mats and Implications for the Archean Stromatolite Record. *Geosciences*, 2(4), pp.235–259.

Simonson, B.M. & Carney, K.E., 1999. Roll-up Structures; Evidence of in Situ Microbial Mats in Late Archean Deep Shelf Environments. *PALAIOS*, 14(1), pp.13–24.

Skidmore, M.L., Foght, J.M. & Sharp, M.J., 2000. Microbial Life beneath a High Arctic Glacier. *Applied and Environmental Microbiology*, 66(8), pp.3214–3220.

Slingerland, R. & Smith, N.D., 1986. Occurrence and Formation of Water-Laid Placers. *Annual Review of Earth and Planetary Sciences*, 14(1), pp.113–147.

Sozinova, O. et al., 2005. A Three-Dimensional Model of Myxobacterial Aggregation by Contact-Mediated Interactions. *Proceedings of the National Academy of Sciences of the United States of America*, 102(32), pp.11308–11312.

Stal, L.J., 1995. Physiological Ecology of Cyanobacteria in Microbial Mats and Other Communities. *New Phytologist*, 131(1), pp.1–32.

Stoodley, P. et al., 1998. Oscillation Characteristics of Biofilm Streamers in Turbulent Flowing Water as Related to Drag and Pressure Drop. *Biotechnology and Bioengineering*, 57(5), pp.536–544.

Sumner, D.Y., 1997. Late Archean Calcite-Microbe Interactions; Two Morphologically Distinct Microbial Communities That Affected Calcite Nucleation Differently. *PALAIOS*, 12(4), pp.302–318.

Swingley, W.D., Blankenship, R.E. & Raymond, J., 2008. Integrating Markov Clustering and Molecular Phylogenetics to Reconstruct the Cyanobacterial Species Tree from Conserved Protein Families. *Molecular Biology and Evolution*, 25(4), pp.643–654.

Taherzadeh, D., Picioreanu, C. & Horn, H., 2012. Mass Transfer Enhancement in Moving Biofilm Structures. *Biophysical Journal*, 102(7), pp.1483–1492.

Taj, R.J., Aref, M.A.M. & Schreiber, B.C., 2014. The Influence of Microbial Mats on the Formation of Sand Volcanoes and Mounds in the Red Sea Coastal Plain, South Jeddah, Saudi Arabia. *Sedimentary Geology*, 311, pp.60–74.

Tanja Bosak, A.H.K., 2012. The Meaning of Stromatolites. *Annual Review of Earth and Planetary Sciences*, 41(1).

The MPlayer Team, 2000. *MEncoder*, Available at: http://www.mplayerhq.hu [Accessed March 5, 2014].

Thielicke, W. & Stamhuis, E.J., 2014. PIVlab - Time-Resolved Digital Particle Image Velocimetry Tool for MATLAB (version: 1.4). Available at: http://figshare.com/articles/PIVlab_version_1_35/1092508 [Accessed May 31, 2015].

Tice, M.M. et al., 2011. Archean Microbial Mat Communities. *Annual Review of Earth and Planetary Sciences*, 39(1), pp.297–319.

Tice, M.M. & Lowe, D.R., 2006. Hydrogen-Based Carbon Fixation in the Earliest Known Photosynthetic Organisms. *Geology*, 34(1), pp.37–40.

Tolhurst, T.J. et al., 2003. Diatom Migration and Sediment Armouring – an Example from the Tagus Estuary, Portugal. *Hydrobiologia*, 503(1-3), pp.183–193.

Underwood, G.J.C., Paterson, D.M. & Parkes, R.J., 1995. The Measurement of Microbial Carbohydrate Exopolymers from Intertidal Sediments. *Limnology and Oceanography*, 40(7), pp.1243–1253.

Vogel, S., 1994. *Life in Moving Fluids: The Physical Biology of Flow*, Princeton University Press.

Walsh, M.W., 1992. Microfossils and Possible Microfossils from the Early Archean Onverwacht Group, Barberton Mountain Land, South Africa. *Precambrian Research*, 54(2–4), pp.271–293.

Walter, M.R., Bauld, J. & Brock, T.D., 1976. Microbiology and Morphogenesis of Columnar Stromatolites (conophyton, Vacerrilla) from Hot Springs in Yellowstone National Park. In M. R. Walter, ed. *Stromatolites*. New York, USA: Elsevier, pp. 273–310.

Wang, Y. et al., 2014. Estimating Rice Chlorophyll Content and Leaf Nitrogen Concentration with a Digital Still Color Camera Under Natural Light. *Plant Methods*, 10. Available at: http://www.ncbi.nlm.nih.gov/pmc/articles/PMC4236477/ [Accessed September 4, 2015].

Westbroek, P., 1983. Life as a Geologic Force: New Opportunities for Paleontology? *Paleobiology*, 9(2), pp.91–96.

de Winder, B. et al., 1999. Carbohydrate secretion by phototrophic communities in tidal sediments. *Journal of Sea Research*, 42(2), pp.131–146.

APPENDIX

A1: Statistical Analysis of Grain Distributions

Sorting patterns in Moodies fossil mats were compared with sorting from experimental mats by normalizing all grain sizes with respect to the grain size mean (ϕ_0) and standard deviation (σ_0) observed outside one full cone width at half maximum height (FWHM), such that $\phi' = (\phi_0 - \phi)/\sigma_0$. All distances were normalized to cone size by dividing by FWHM (full-width at half cone-height maximum) such that $d = D/FWHM$. Dummy variables were defined as:

$$u_i = \begin{cases} 1 & \text{if grain is observed in sample i} \\ 0 & \text{otherwise} \end{cases}$$

A simple multilinear regression of ϕ' on d, u_i and $u_i \cdot d$ for all samples was then performed:

$$\phi' = m + a_0 \cdot d + a_1 \cdot u_1 + a_2 \cdot u_2 + a_3 \cdot u_3 + b_1 \cdot u_1 \cdot d + b_2 \cdot u_2 \cdot d + b_3 \cdot u_3 \cdot d + \varepsilon ,$$

where *m*, a_i, and b_i are regression coefficients and ε is the regression error. Note that no dummy variable or interaction term was included for the experimental data in order to avoid perfect colinearity in the dummy terms. This regression effectively compared the Moodies fossil cones to the experimental cones as a baseline, with a significant difference in sorting relationship detected if any a_i or b_i was significantly different from 0. Student t-tests on all of a_i and b_i indicated no significant differences, with *p(t)* = 0.058-0.083 for all a_i and *p(t)* = 0.48-0.76 for all b_i. Although *p(t)* values for coefficients on the dummy terms (a_i) approach significance at the 95% confidence level, these terms

reflect small differences in the regression intercepts which are likely sensitive to the varying distances from cone centers over which grains were measured. Far more important are the interaction terms (b_i) which indicate that relative grain sorting was accomplished over similar distances of travel up cone slopes.

A2: Estimation of Force Necessary to Initiate Rolling of Sand Grains

For simplicity and in order to obtain an order-of-magnitude estimate of the force necessary to roll a sand grain over a bed of smaller grains, a 2-D model was constructed assuming a sphere rolling over two smaller spheres. In this model, the weight of the grain (F_g) acts on the center of the grain and is balanced by the force generated by the bacteria (F_b) at the top of the upper grain. These forces generate opposing torques (τ_g and τ_b) about the point of contact between the overlying grain and one of the underlying grains.

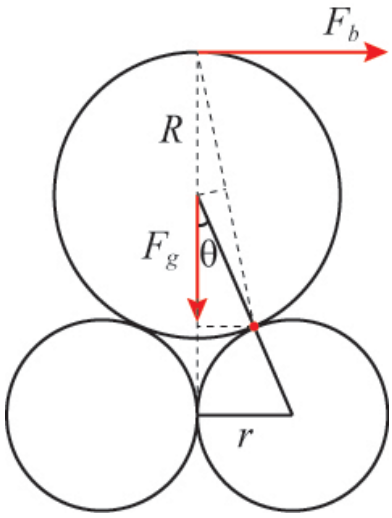

Figure A2. Torque balance diagram to calculate the force necessary to initiate the rolling of a sand grain on top of existing grains.

$\tau_g = mgR\sin(\theta) = \frac{mgRr}{R+r}$, where m is the mass of the sphere on top. g is the gravitational acceleration of Earth. R and r are the radii of the spheres above and below, respectively.

$$\tau_b = F_b \cdot 2R\cos(\frac{\theta}{2})\cos(\frac{\theta}{2}) = F_b \cdot R\left[1+\frac{\sqrt{R^2+2Rr}}{R+r}\right]$$

Setting $\tau_g = \tau_b$ and solving for F_b, we obtain the following required minimum force to initiate sand grain rotation:

$$F_b = \frac{mg}{1+x+\sqrt{x^2+2x}} = \frac{\frac{1}{6}\pi\rho_{eff}D^3 g}{1+x+\sqrt{x^2+2x}},$$

where $m = \frac{4}{3}\pi\rho_{eff}R^3$, $x = \frac{R}{r}$, $D = 2R$ and ρ_{eff} =1.7×10^3 kg m^{-3} for sand submerged under water.

A3: Cone Scaling Model

We model the growth and spatial organization of cones as a function of the motility of Leptolyngbya tufts. This model assumes that mat growth has already progressed to a stage at which mobile cones have started to form but are not generally in contact with one another through star arms. Under this conditions, cones can be modelled as the sticky aggregation of organisms with density ρ that execute two-dimensional random walks with an average velocity in any direction of u. We make the mean field approximation that these cones encounter individuals, tufts, and other cones at a rate determined by the average surface density, σ, of organisms present in the mat as a whole. Then the rate of growth of a cone with mass m and radius r is

$$\frac{\mathrm{d}m}{\mathrm{d}t} = 2ru \cdot \sigma , \qquad (1)$$

where 2ru is the area per unit time swept by cones moving across the sediment surface.

Assume cones have constant slopes with masses described by

$$m = \frac{1}{3}\pi r^2 h \cdot \rho\alpha = \frac{\alpha}{3}\rho\pi r^3 s , \quad (2)$$

where r is the radius at the base of the cone, h is the height, s is the slope of the cone surface, and α is a constant between 0 and 1 describing the fractional volume of the bounding cone occupied by centers and radiating star arms. Substituting for m in equation 1 yields the following relationship for the rate of growth of cones during the day:

$$\frac{\mathrm{d}r}{\mathrm{d}t} = \frac{2\sigma u}{\pi s \rho \alpha} \cdot \frac{1}{r} \qquad (3)$$

The solution to equation 3 is

$$r = \sqrt{4D\left(t - t_0\right) + r_0^2}\ , \quad (4)$$

where we define $D = \dfrac{\sigma u}{\pi s \rho \alpha}$.

If cones grow by aggregation during the day (growing time T), partially disaggregate during the evening, and partially reconstitute the following morning such that $r_{morning} = \beta r_{evening}$, then after n day-night cycles the average cone radius can be estimated as

$$r_n = \sqrt{\frac{4DT\left(1-\beta^{2n}\right)}{1-\beta^2}}, \qquad (5)$$

where β is the average fraction of cells that do not disaggregate at night.

By defining an effective diffusivity, $D_{eff} = D/(1-\beta^2)$ and solving for the asymptotic radius approached by cones over n days, the limiting size of cones as $n \to \infty$ becomes:

$$r_\infty = \sqrt{4D_{eff}T}\ , \qquad (6)$$

which suggests that the average cone spacing scales as a characteristic diffusive length in 2D(Berg 1993). In particular, cone size and spacing are proportional to the square root of illuminated daylight time.

By examining the time for cones to approach limiting size, this model also revealed some interesting dynamics on the conical mat formation. For example, with $\beta < 0.9$, the average spacing of cones is expected to approach the limiting size of r_∞ in

less than eight days. For $\beta = 0.5$, or the approximate inheritance observed in our experiments, limiting size is approached in just two days. This rapid approach to final cone size is observed in our experiments.

Calculations also show that, with the average cone spacing (r_∞) from one of our experiments at 3 mm (Figure S2), the corresponding effective diffusivity (D_{eff}) for a 12-hour day growth is 5×10^{-11} m^2 s^{-1}. In comparison, the diffusivity of dissolved CO_2 is 3×10^{-9} m^2 s^{-1} at the growth temperature. Clearly, D_{eff} from this order of magnitude estimate depends on a range of parameters, each of which could vary. The low, high and best estimates (that match with our experimental observation) may be summarized in the following table (Table. S1). From this calculation, although the effective diffusivity could vary by three orders of magnitude, the corresponding diffusive length scales (cone radius) are within one order of magnitude, with values consistent with our experimental observation.

Parameters for D_{eff}	**Estimates**			**Unit**
	LOW	**BEST**	**HIGH**	
Surface density (σ)	10000	10000	10000	cells / mm^2
Group velocity (u)	0.001	0.005	0.01	mm/s
Fractional density (α)	0.1	0.1	0.1	1
Slope (s)	1	0.7	0.1	1
Density (ρ)	1.0E+07	1.0E+07	1.0E+07	cells / mm^3
Inheritance (β)	0.1	0.5	0.9	1
Effective Diffusivity:	6.43E-12	6.06E-11	3.35E-09	m^2/s
Predicted Cone Radius:	1.05	3.24	24.06	mm

Table. A3.1. Estimates of model parameters that were used to calculate the effective diffusivity and the predicted cone radius.

More broadly, this model also correctly predicts the centimetre-scale size and spacing for cones in a wide variety of modern and ancient examples (A. P. Petroff et al. 2010) given realistic model parameters (Table. A3.1). Since the limiting size is relatively insensitive to different values of β except in cases of very large inheritance of cone size from evening to morning (which was not observed during this study), we assume $\beta = 0.1 – 0.9$ and $T = 1 – 4 \times 10^4$ s (12 hours). These assumptions result the limiting average cone size about 2-30 mm, and the limiting spacing 4-70 mm for densely packed cones. These size ranges are commonly observed in the geologic record of fossilized conical mats (A. P. Petroff et al. 2010).

Our model thus demonstrated that by simple assumptions of coupled growth and motility, transport and spatial organization of bacterial biomass can mimic diffusive processes, producing features scalable to diffusive length scales. Although the spacing and geometry of cones are clearly influenced by the physical laws that govern diffusion, biological processes such as motility still play an important role.

A4: Fluid-Structure Interaction Model for Streamer Initialization

The goal for constructing this model is to simulate the interactions between fluid flow and the deformation of a surface-attached elastic solid, as a first step towards simulating the interaction between fluid forcing and the resulted deformation in microbial mats. The geometry of the model space was generated an open source program Gmsh (Geuzaine & Remacle 2009), in which two different domains corresponding to the fluid and the solid were labeled and imported to deal.II.

The *fluid* domain is assumed to be under laminar flow, described using time independent Stoke's Equation:

$$-2\eta \nabla \cdot \varepsilon(v) + \nabla p = 0,$$

$$-\nabla \cdot v = 0 \text{ in } \Omega_{fluid}$$

The *solid* domain assumes a simple elasticity equation:

$$-\nabla \cdot C\varepsilon(u) = 0 \text{ in } \Omega_{solid} \quad ,$$

where ε is the strain tensor represents elastic deformation, v the fluid velocity and u the displacement of the solid. η is the viscosity of the fluid and p the pressure. C is the elasticity tensor for the solid. The surface topography will takes arbitrary forms where *No-Slip* condition applies (v=0 at the fluid-solid interface).

The model takes realistic (dimensional) physical parameters. This is so that it provides quick physical insights. The simulation space is a rectangle of length 20 mm and height 7.5 mm (Figure A4.1). The thickness of the biofilm is 0.5 mm. During simulation, fluid velocity is set at 0.3 m/s and the viscosity of the fluid is 0.894e-3 Pa·s.

For the property of microbial mats, we set $\lambda = \mu = 50$ Pa, where λ and μ are lame's first and second parameter (lame's parameters are used to construct *C*).

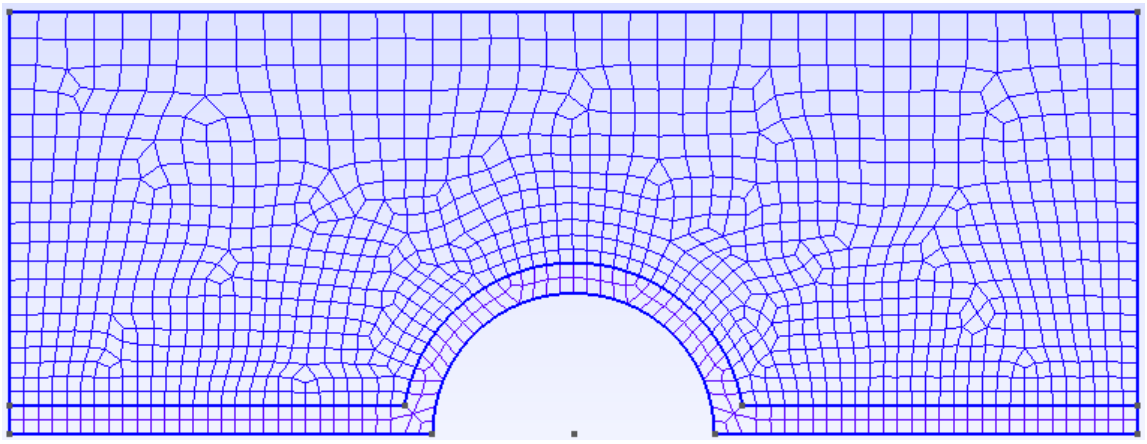

Figure A4.1. Simulation space for the finite element fluid-structure interaction model. Top: fluid domain. Bottom (adjacent to the surface): elastic solid domain.

The C++ code in deal.II was adapted based on the tutorial program step-46, with the mesh-import component based on step-49. Realistic physical parameters such as spatial dimensions, coefficients of elasticity and viscosity were also used. This program computes the deformation of the solid in discrete steps. However, each step was treated as a time-independent problem in order to approximate a time-dependent problem. The mesh deformation scheme is followed in step-18, within which each finite element is moved to simulation a real deformation process.

A4.1 Gmsh code

The following mesh text file (mats.geo) was created, representing a 2D fluid-interaction geometry where a thin layer of solid is sitting on a local roughness element (a half circle) underneath a fluid.

– mats.geo –

```
Mesh.Algorithm = 8;
Mesh.RecombineAll = 1;

es_fluid    = 0.05;
es_mat      = 0.025;
es_boundary = 0.025;
sp          = 0.01;
Point(1) = {2*sp, 0.75*sp, 0*sp, es_fluid*sp};
Point(2) = {0*sp, 0.75*sp, 0*sp, es_fluid*sp};
Point(3) = {2*sp, 0*sp, 0*sp, es_mat*sp};
Point(4) = {0*sp, 0*sp, 0*sp, es_mat*sp};
Point(5) = {0.75*sp, 0*sp, 0*sp, es_mat*sp};
Point(6) = {1*sp, 0*sp, 0*sp, es_mat*sp};
Point(7) = {1.25*sp, 0*sp, 0*sp, es_mat*sp};
Point(8) = {0*sp, 0.05*sp, 0*sp, es_boundary*sp};
Point(9) = {0.7*sp, 0.05*sp, 0*sp, es_boundary*sp};
Point(10) = {1.3*sp, 0.05*sp, 0*sp, es_boundary*sp};
Point(11) = {2*sp, 0.05*sp, 0*sp, es_boundary*sp};
Line(1) = {1, 2};
Line(2) = {1, 11};
Line(3) = {11, 3};
Line(4) = {2, 8};
Line(5) = {8, 4};
Line(6) = {4, 5};
Line(7) = {3, 7};
Line(8) = {8, 9};
Line(9) = {11, 10};
Circle(10) = {7, 6, 5};
Circle(11) = {10, 6, 9};
Line Loop(12) = {1, 4, 8, -11, -9, -2};
Plane Surface(13) = {12};
Line Loop(14) = {6, -10, -7, -3, 9, 11, -8, 5};
Plane Surface(15) = {14};
Physical Line(16) = {1};        // Top
Physical Line(17) = {4};        // Left Fluid
Physical Line(18) = {5};        // Left Mat
Physical Line(19) = {2};        // Right Fluid
Physical Line(20) = {3};        // Right Mat
Physical Line(21) = {10, 6, 7}; // Bottom
Physical Surface(24) = {13};    // Fluid Domain
Physical Surface(25) = {15};    // Solid Domain
```

This Gmsh file is then imported into Deal.II using the make_grid() function. Specifically, the *id_2d_fluid_domain* and *id_2d_solid_domain* are two numerical values corresponding to the Physical Surface object within Gmsh.

```
template <int dim>
void
FluidInteraction<dim>::make_grid ()
{
  GridIn<dim> gridin;
  gridin.attach_triangulation(triangulation);
  std::ifstream f(InputMeshFileName);
  gridin.read_msh(f);

  mesh_info(triangulation, OutputMeshFileName);

  // Setting Material IDs
  for (typename hp::DoFHandler<dim>::active_cell_iterator
```

```
        cell = dof_handler.begin_active();
        cell != dof_handler.end(); ++cell)
    if ( cell->material_id() == id_2d_fluid_domain )
      cell->set_material_id (fluid_domain_id);
    else if ( cell->material_id() == id_2d_solid_domain )
      cell->set_material_id (solid_domain_id);
    else
      Assert (false, ExcNotImplemented());
}
```

A4.2 Boundary Conditions

With complex geometry imported from Gmsh, the boundary conditions were assigned on all the boundary faces within the `setup_dof ()` function with the following code block:

```
    // TOP Fluid
    VectorTools::interpolate_boundary_values (dof_handler,
                                              id_2d_fluid_top_boundary,
                                              StokesBoundaryValues<dim>(),
                                              constraints,
                                              fe_collection.component_mask(velocities));

    // LEFT Fluid - Poiseuille Flow Boundary Condition
    VectorTools::interpolate_boundary_values (dof_handler,
                                              id_2d_fluid_left_boundary,
                                              StokesBoundaryValues<dim>(),
                                              constraints,
                                              fe_collection.component_mask(velocities));

    // RIGHT Fluid - Poiseuille Flow Boundary Condition
    VectorTools::interpolate_boundary_values (dof_handler,
                                              id_2d_fluid_right_boundary,
                                              StokesBoundaryValues<dim>(),
                                              constraints,
                                              fe_collection.component_mask(velocities));

    const FEValuesExtractors::Vector displacements(dim+1);
    // LEFT Solid
    VectorTools::interpolate_boundary_values (dof_handler,
                                              id_2d_solid_left_boundary,
                                              ZeroFunction<dim>(dim+1+dim),
                                              constraints,
                                              fe_collection.component_mask(displacements));

    // RIGHT Solid
    VectorTools::interpolate_boundary_values (dof_handler,
                                              id_2d_solid_right_boundary,
                                              ZeroFunction<dim>(dim+1+dim),
                                              constraints,
                                              fe_collection.component_mask(displacements));
    // BOTTOM Solid
    VectorTools::interpolate_boundary_values (dof_handler,
                                              id_2d_solid_bottom_boundary,
                                              ZeroFunction<dim>(dim+1+dim),
                                              constraints,
                                              fe_collection.component_mask(displacements));
```

In particular, the interpolate_boundary_values calls the `StokesBoundaryValues<dim>()` function, which was modified to take into account for the Poiseuille Flow condition at left and right boundary:

```
template <int dim>
double
  StokesBoundaryValues<dim>::value (const Point<dim>  &p,
                                    const unsigned int component) const
{
  Assert (component < this->n_components,
          ExcIndexRange (component, 0, this->n_components));

  if (component == 0)
    return Vel_top_x*(2*(Thickness_FlowMat-Thickness_Mat)*(p[1]-Thickness_Mat)
                                    -(p[1]-Thickness_Mat)*(p[1]-Thickness_Mat))
         /((Thickness_FlowMat-Thickness_Mat)*(Thickness_FlowMat-Thickness_Mat));
  else
    return 0;
}
```

Next, the Right Hand Side values are also modified to include gravity:

```
template <int dim>
double RightHandSide<dim>::value (const Point<dim>  &p,
                                  const unsigned int component) const
{
  Assert (component < this->n_components,
          ExcIndexRange (component, 0, this->n_components));

  if (component == dim -1)
    return -density_water * grav_const;
  else
    return 0;
}
```

Relevant changes are updated from the step-46 `assemble_system ()` function in order to implement the Right Hand Side properly.

A4.3 Moving Mesh

Another addition to the program is a local scheme to move the cells (deformation) according to the solution. This is achieved with the `move_mesh ()` function, shown below in the code block:

```
template <int dim>
void
FluidInteraction<dim>::move_mesh ()
{
  std::vector<bool>  vertex_touched (triangulation.n_vertices(), false);
  std::vector<float> fe_degrees (triangulation.n_active_cells());

  for (typename hp::DoFHandler<dim>::active_cell_iterator
         cell = dof_handler.begin_active ();
         cell != dof_handler.end(); ++cell )
    for (unsigned int v=0; v<GeometryInfo<dim>::vertices_per_cell; ++v)
      if (vertex_touched[cell->vertex_index(v)] == false )
        {
          if( cell_is_in_solid_domain(cell) ) // only move the cells in the solid domain
          {
            vertex_touched[cell->vertex_index(v)] = true;

            Point<dim> vertex_displacements;
            for (unsigned int d=0; d<dim; ++d)
              vertex_displacements[d]
                = solution(cell->vertex_dof_index(v,d,cell->active_fe_index()));

            cell->vertex(v) += vertex_displacements;
          } else if ( cell_is_in_fluid_domain(cell) )
          {
            // figure out a way to move the fluid cells
          }
        }
}
```

A5: Linear Flume Design and PIV Setup

This linear flume was designed and constructed per discussions with Dr. Scott A. Socolofsky at Texas A&M University. The flume was constructed almost entirely with polycarbonate sheets cut to precision parts with a table-saw and welded together with polycarbonate solvents. Machined shapes were manufactured in the Mechanical Engineering machine shop. Upon recirculating water through two pumps, the flow is conditioned through a 10 cm long, straight glass flow-straightener. This forces the flow to stabilize quickly. When fluid flows pass the mid-section of the flume, it is generally well characterized and the flow is most stable under the sheet laser towards the end. At the end, the flow height can also be controlled through a height regulator before going back to the reservoir and being recirculated again (Figure A5.1).

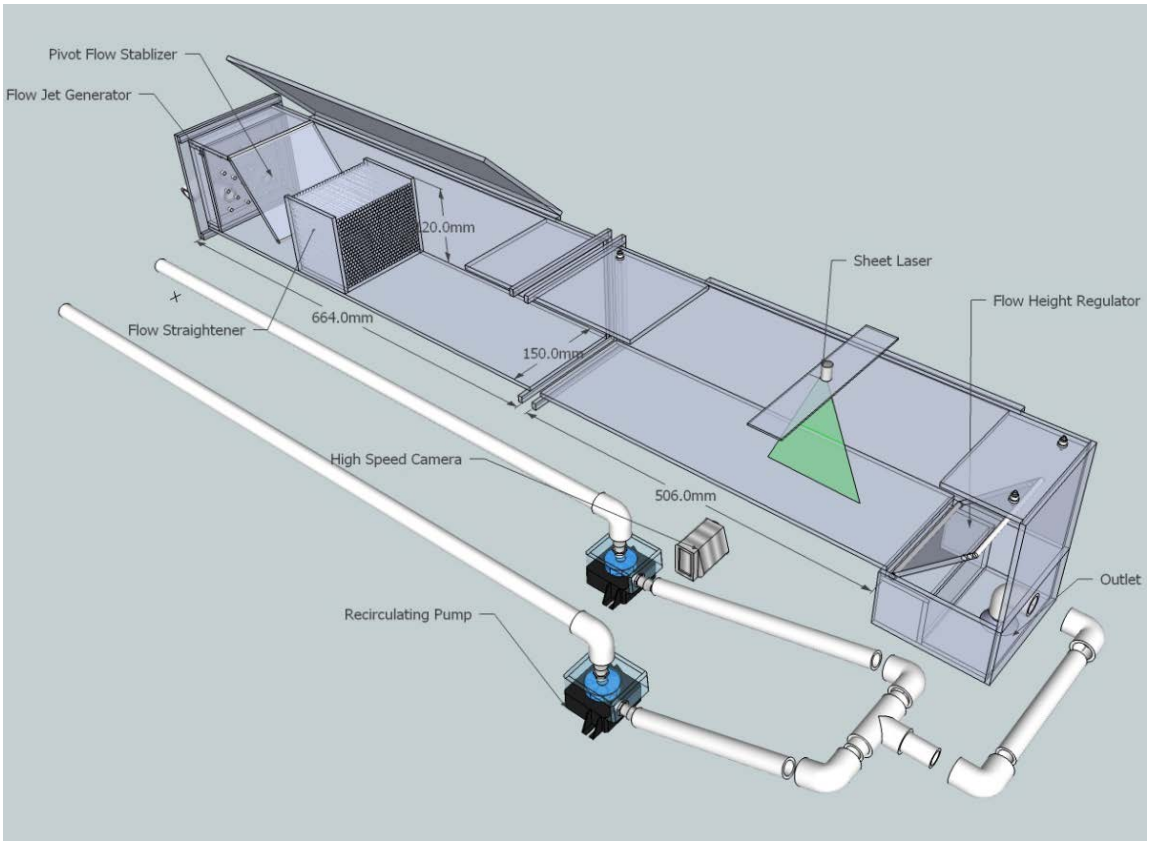

Figure A5.1. Linear Flume Design and PIV Setup

A6: Circular Flume Reactor Design

The circular flow flume reactor is an enclosed glass bioreactor with nutrients and air pumped in and out. Flow is created by magnetically controlling the stir of a magnet at the bottom of the reactor. A plate is designed with an open hole at the center, which allows the vertex of the flow to transfer through. At the rate of stirring about 400 rpm maximum (stir bar becomes unstable at higher speeds), a characteristic flow speed of about 2-4 cm per second at the half-radius of the disk can be reached. This flow is well-characterized through PIV analysis (data not shown). The diameter of the plate is approximately 18 cm.

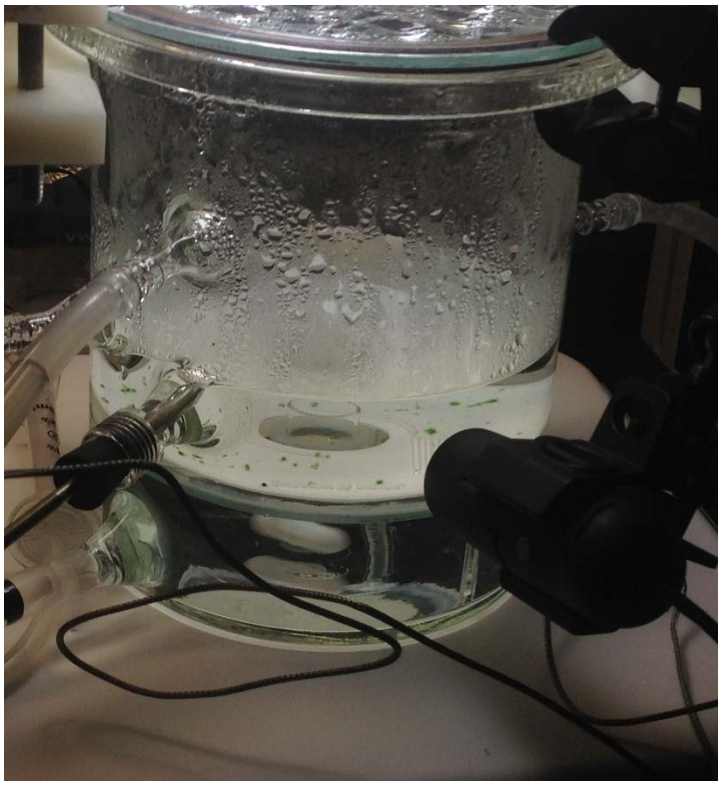

Figure A6.1. Circular Flow Flume Reactor.

A7: Growth Tube Design

Cyanobacteria cultures were grown in modified 10 mL sterile syringe tubes (Figure A7.1). The tubes were designed with an open top to the atmosphere through a 0.22 micron mesh filter, for the purpose of blocking out other bacterial contaminations while still allowing gas exchange. Acid washed, autoclaved quartz sand (5 mm thick) were first deposited on top of a 5 mm solid agar layer. The purpose of the agar layer was to assist sand extraction after the removal of the rubber stopper. The bottom of the tube was sealed with a rubber stopper. After adding growth medium to 30 mm thick, the specific cyanobacteria was inoculated. Then the top of the tube is sealed with the mesh filter as the last step. For Leptolyngbya, the tubes were incubated at 42 °C with regular, 12 hour-day, 12 hour-night day-night cycles. Lights were adjusted for maximum growth at around 800-1000 lux using full-spectrum fluorescence light bulbs.

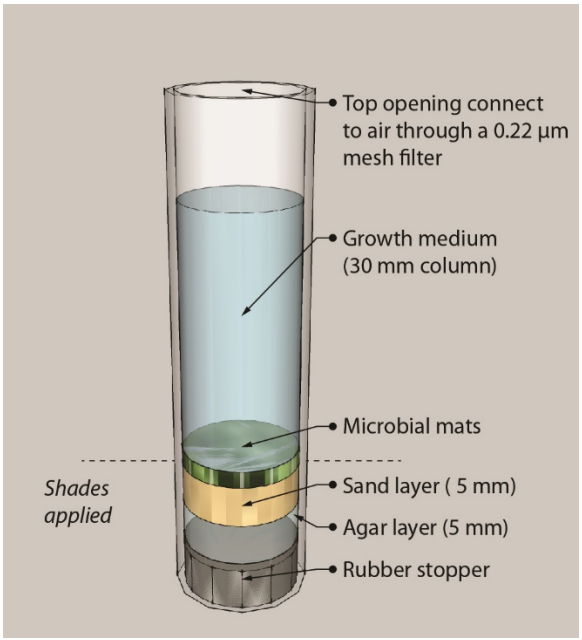

Figure A7.1. Growth tube design. Note that during growth, shades are applied below the top of sand layer. This minimizes growth on side walls below the sand-water interface.

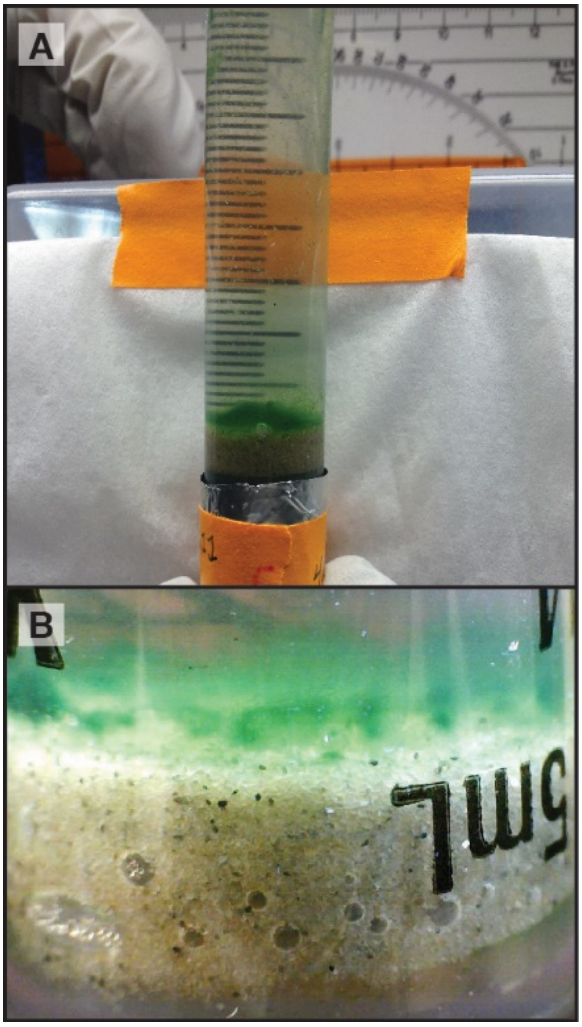

Figure A7.2. Growth of Leptolyngbya in tubes. (A) Whole view. (B) Close-up view of the mats layer.

A8. Robotic Tilting Measurements

A microcontroller-controlled sediment tube tilting apparatus was developed to consistently tilt sediments at constant angular rates while keeping track of the behavior of the sediment. High Definitions videos were taken during the tilt in order to capture the sediment movement. Two sample tubes (one is the abiotic control) were being tilt at all times (Figure A8.1). The controller box (Figure A8.2) provides reliable turning of the motor every time.

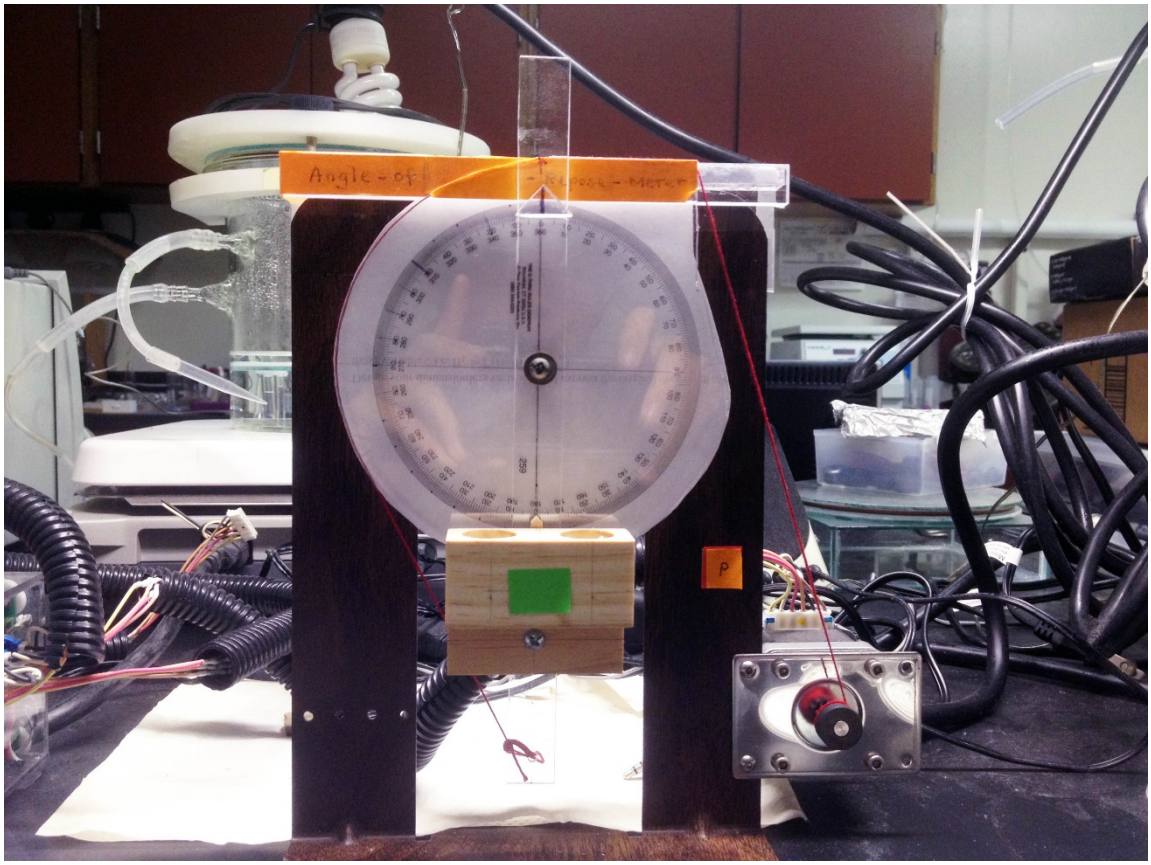

Figure 10.1. Robotic sediment tube tilting apparatus.

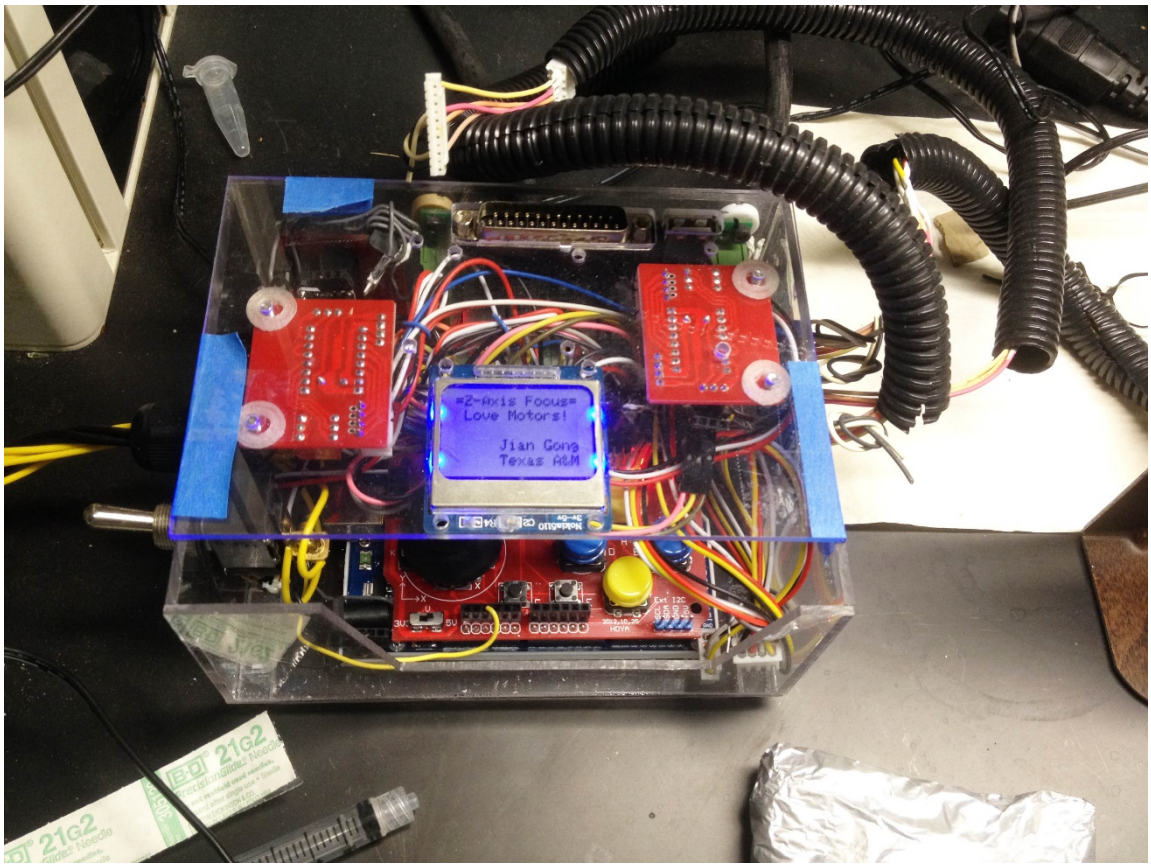

Figure A8.2. Controller unit for the microcontroller.

A9: Protocol: Chlorophyll-a Extraction and Measurement

Preparation:

Make neutralized ethanol solution by adding 0.3 g $MgCO_3$ into 1 L Ethanol (must be non-denatured, 96% concentration best or labelled 190-proof, commonly available in stockrooms which is 95%), allow time for dissolution and filter the mixture with filter paper. Note: All steps below are to be performed under minimal light (to prevent degradation of chlorophyll)

Steps:

1. Add sediment/biological samples together with 6 mL ethanol in each 15 mL centrifuge tubes (VWR), shake by hand.
2. Place tubes with loose cap on in a 78 °C water bath for 5 min (alcohol boils around 78.4 °C). Make sure to secure the tubes well. This weakens the cell membranes and should start to dissolve chlorophyll-a into the alcohol.
3. Remove the tubes, close the caps tight and shake horizontally on a shaker/vortex for 20 min. OR, as an alternative, place the tubes in dark 4 °C cold room overnight (>12 hours). The cold room method takes longer but generally gives better results, therefore single extraction is acceptable. The shaker/vortex method is faster but may require a second extraction step.
4. Centrifuge at 4000 rpm for 10 min.

Now the sample is ready for spectrophotometer analysis. After analysis, pipette out and save the liquid phase of the mixture and do a second extraction with the sample and same tube, by repeating step 1-4.

Measurements:

Use neutralized ethanol as blanks for the spectrophotometer.

1. Measure @ 665 nm and 750 nm, record as A_{665} and A_{750}.

2. Total chlorophyll-a amount can be determined as:

$$\textbf{Chl-a[ug]} = 11.9035 \times [(A_{665} - A_{750})] \times V_{ethanol}\textbf{[mL]} / \textbf{L[cm]}$$

where $V_{ethanol}$ is the ethanol used for extraction. $V_{ethanol}$ = 6 mL in this experiment. L is the path-length for the cuvette used. L = 1 cm for standard cuvettes (used for this experiment) (Ritchie 2006).

A10: Protocol: EPS (Carbohydrate) Extraction and Measurement

EPS (carbohydrate) was be quantified primarily with two methods in this study: (I) Phenol-sulfuric acid method and (II) 96-well plate method, which is based on the same phenol reaction with monosaccharides. Method I utilizes a spectrophotometer and is generally more precise. It is also more flexible to be able to read at different frequencies. However, it requires a large amount of sample (~1 mL) and reagent material. Method II can only take a fixed wavelength and not very precise but it is quick and only requiring a tiny amount of sample and reagent material. More experiment replications can fit on one plate with Method II and essentially all measurements can be performed at once.

Method I: Phenol-Sulfuric Acid Extraction

Preparation:

- 5% phenol solution (shake before use)
- Concentrated sulfuric acid (use caution when handling this!)
- Wide tip pipette (5 mL volume minimum) and 15 mL glass test tubes

Steps:

Perform the following steps in a hood.

1. Prepare 0.5 mL extracted EPS liquid, mix with 1 mL phenol solution.

2. With a cap on, mix 10 sec on a vortex mixer

3. Add 2.5 mL of conc. H_2SO_4. The quality of mixing is essential for this step of analysis. Add all of the sulfuric acid in one continuous, quick step. After adding the

sulfuric acid, the liquid will get hot so never hold the test tube with hand. Make sure the method is consistent with all the samples being measured.

4. Wait 10 minutes, take the measurement at 490 nm with a spectrophotometer.

Use the same method to produce a calibration curve for D-glucose at 0, 20, 40, 60, 80 and 100 µg/m. The measured absorbance for the sample will then be reported in glucose-equivalent units.

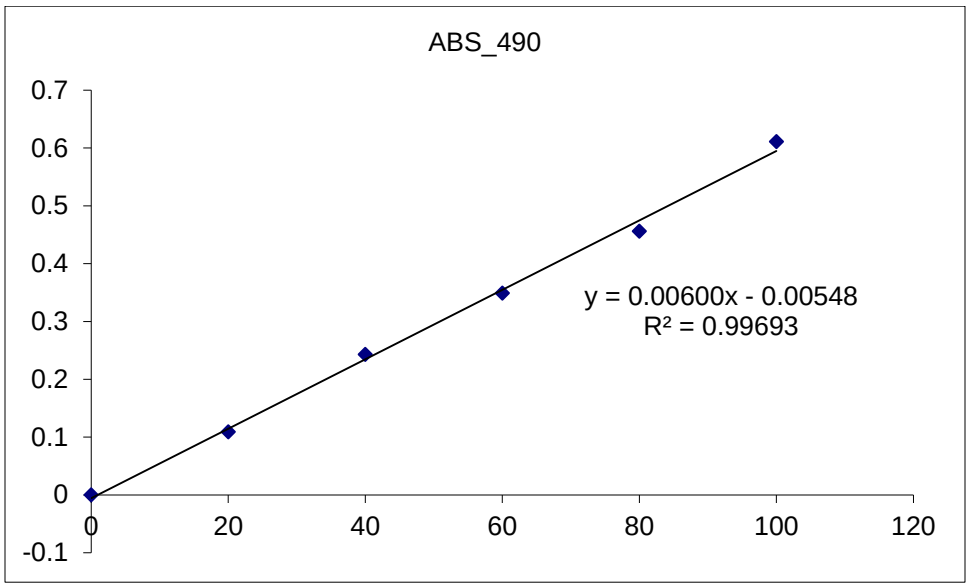

Figure A10.1. Example calibration curve used for one set of experiments. Note: calibration was redone for each set of experiment.

Method II: 96-Well Plate Method for Carbohydrate Extraction

Preparation:

- Concentrated H_2SO_4 (dangerous, use caution).
- 5% phenol solution (respiration hazard, operate within hood).
- For the 96-well plate method, prepare a 90 °C water bath as well as a room temperature water bath (20-25 °C)

Note: Specification of standard 96-well plates: single well volume (25-340 µL), maximum sample 360 µL.

Steps:

1. Use a pipette, prepare 50 µL sample for analysis. Carefully pipette the sample into one well. Let the pipette tip touch the wall towards the bottom so that water-tension may absorb all of the sample in one bead during transfer.
2. Add 150 µL conc. H_2SO_4 while assist mixing by pipetting up and down for 10 times.
3. Add 30 µL, 5% phenol solution. Place a magnetic stir bar in the phenol solution, take the phenol solution while the stirring.
4. Add controls and blank samples in the wells in the same fashion.
5. Immediately (as soon as you can) place the plate in 90 °C bath, carefully let the plate float on its own. Float for 5 minutes.
6. Cool the plate for another 5 minutes in a room water bath (20-25 °C).

Measurements:

Before measurements, perform a wavelength scan to determine the composition of polysaccharides. This information is reflected on the position of the peak around 490 nm. Glucose is at 490 nm, while other monosaccharides could show shifted peaks typically from 480 nm to 495 nm. Measure absorbance at 490 nm if the polysaccharide is glucose based. Use the same method to produce a calibration curve for D-glucose at 0, 20, 40, 60, 80 and 100 µg/mL. The measured absorbance for the sample will then be reported in glucose-equivalent units.

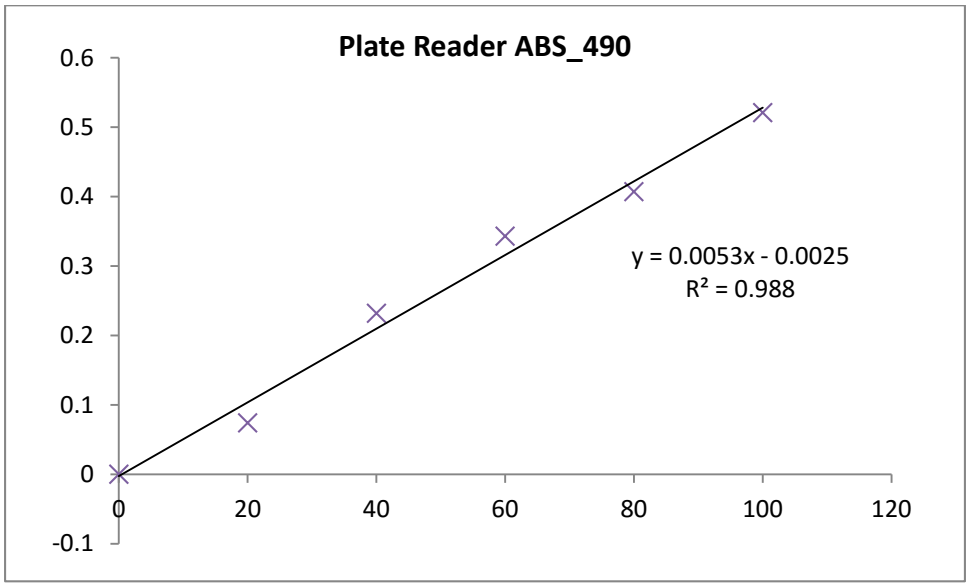

Figure A11.2. Example calibration curve for the plate reader method. Note: this method uses less material but has relatively large uncertainty, therefore more replications (at least 5) are suggested.

A11: Multiple Mann-Whitney Tests for Variations in Mat Strength

In order to maintain a family-wise error rate of 0.05, a significance threshold of $\alpha = 0.0085$ was chosen for pair-wise testing (Šidàk correction).

Mat group	≥2.65 Ga	Cuspate mats	2.65–0.10 Ga	Modern
≥2.65 Ga	–			
Cuspate mats	$U = 40$; $P = 0.002$*	–		
2.65–0.10 Ga	$U = 235$; $P = 5.9\times10^{-5}$*	$U = 83$; $P = 0.061$	–	
Modern	$U = 53$; $P = 0.274$	$U = 32$; $P = 0.004$*	$U = 171.5$; $P = 0.0044$*	–

* Significantly different distributions at $\alpha = 0.0085$ (family-wise Type I error rate of 0.05)

Table A11. Multiple Mann-Whitney tests for variations in mat strength

A12: Color Index Development and Test Results

Color Index	Pearson Correlation	Significance (p-value)
Norm_R (r)	-0.885	0.000132691
Norm_G (g)	0.935	8.31466E-06
Norm_B (b)	-0.746	0.00536877
g/r	**0.959**	**8.10759E-07**
g/(r*b)	0.930	1.1759E-05
g/(r+b)	0.938	6.39E-06

Table A12. Development of a color index to correlate with laboratory chlorophyll-a measurements. Note: R, G and B are total sums of pixel intensity in the image and r = R/(R+G+B). g = G/(R+G+B) and b = B(R+G+B), which are normalized pixel color intensity.

A13: Extended Mat Strength Data Table

Age (Ma)	Unit	Cohesion (Pa)	Tensile strength*tan(30) (Pa)	Method*	Width (cm)	Layer thickness (mm)	Reference
3.426	Strelley Pool Chert	8.5		S	9.8	3	Allwood et al., 2009; Fig. 2
3.412	Buck Reef Chert		0.87	D			Tice et al., 2011
3.2	Moodies Group	1		R			Noffke et al., 2006
3.2	Moodies Group	0.5		G			Tice, personal collection
2.98	Nsuze Group	4.6		S	12.8	4	Tice, et al., 2011; Fig. 4B
2.9	Nsuze Group	1		R			Noffke et al., 2008
2.8	Sebakwian Group	1.9		S	1.9	1.1	Orpen & Wilson, 1981; Fig. 3
2.728	Joutel Volcanic Complex		51.4	D			Hofmann and Masson, 1994; Fig. 2C
2.715	Tumbiana Formation	6.9		S	10.6	14	Sakurai et al., 2005; Fig. 10F
2.715	Klippan Formation	2.7		S	2.6	6.8	Buck, 1980; Fig. 7A
2.65	Cheshire Fm	2		S	5	3.4	Pope, personal collection
2.63	Carrawine Dolomite	5.1		S	7.2	5.7	Murphy & Sumner, 2008; Fig. 4B
2.642	Schmidtsdrift Formation	13.7		S	0.5	1	Bertrand-Sarfati and Eriksson, 1977; Fig. 15
2.6	Bulawayo Greenstone Belt		27.7	T			Sumner, 2000; Fig. 3
2.521	Campbellrand	19.6		S	11	17.6	Beukes, 1987; Fig. 5A
2.521	Fairfield Formation		12.7	T			Sumner, 2000; Fig. 4
2.521	Gamohaan Formation		39.8	D			Sumner, 1997; Fig. 9A
2.2	Hurwitz Group	3.6		S			Hofmann and Davidson, 1998; Fig. 5
2.2	Juderina Formation	7		S			Grey, 1994; Fig. 4A

2.14	Abner Formation	10.3	S			Hoffman and Grotzinger, 1988; Fig. 5A
2	Monteville Formation	28.6	S			Bertrand-Sarfati and Potin, 1984; Fig. 9
1.9	Beechey Formation	26.9	S			Pelechaty and Grotzinger, 1988; Fig. 9C
1.9	Albanel Formation, Canada	40.1	S			Hofmann, 1977; Figure 2B
1.8	Rocknest Formation	32.1	S			Pope, personal collection
1.8	Talthelei Formation	35.2	S	33	120	Hoffman, 1974; Fig. 7
1.8	Great Slave Lake Group	7.2	S			Pannetta, 1976; Fig. 1
1.8	Kuuvik Formation	34.4	S			Pope, personal collection
1.65	Earheedy Group, Australia	12.2	S			Grey, 1984; Plate 10A
1.5	Bil'yakh Group	11.1	S			Knoll, 2003; Fig. 7.4
1.4	Lr Missoula Group, Belt Sgp	11.7	S			Horodyski, 1975; 14C
1.4	Altyn Ls., Belt Supergroup	23.2	S			Horodyski, 1983; 20C
0.89	Derevnya Formation	18.8	S			Serebryakov, 1976; Fig. 6
0.85	Little Dal Group	6.5	S			Batten et al., 2004; Fig. 4B
0.75	Backlundtoppen Formation	4.1	S			Knoll et al., 1989; Fig. 10-6
0.63	Nsc3 Formation, Gabon	8	S			Preat et al., 2010; Plate 1D
0.6	Canyon Formation	0.2	S			Fairchild, 1991; Fig. 3A
0.5	Dotsero Formation	27.8	S			Campbell, 1976; Fig. 8
0.45	Eureka Quartzite	17.4	S			Druschke et al., 2009; Fig. 5C
0.25	Union Wash Formation	6.2	S			Mary and Woods, 2008; Fig. 6A

0.245	Virgin Limestone Member	30.5	S			Pruss and Bottjer, 2004; Fig. 4A
0	Lake Untersee	3.6	S			Geobiology in press
0	Yellowstone (Conophyton Pool)	0.3	S			Walter et al., 1976; Fig. 24
0	Shark Bay	8.2	S	20.9	20.9	Chivas et al., 1990; Fig. 2
0	Highborne Cay	1.9	S	6.6	4.6	Reid et al., 2000; Fig. 1B
0	Isle of Sylt	2.7	E			Tolhurst et al., 1999
0	Westerschelde Estuary	7.3	E			Tolhurst et al., 2006
0	Experimental	4	E			Tolhurst et al., 2008
0	Experimental	12.7	E			de Brouwer et al., 2005

*S = slope; E = erosion; D = drape; R = sedimentary structure; G = detrital grain

Table A13. Extended mat strength data table and references.